Dynamic control of X-ray core-exciton resonances by Coulomb screening in photoexcited semiconductors Supporting Information

Thomas C. Rossi*[1], Lu Qiao*[2], Conner P. Dykstra[3], Ronaldo Rodrigues Pela[4], Richard Gnewkow[1,5], Rachel Wallick[3], John H. Burke[3], Erin Nicholas[3], Anne-Marie March[6], Gilles Doumy[6], D. Bruce Buchholz[7], Christiane Deparis[8], Jesus Zuñiga-Pérez[8,9], Michael Weise[10], Klaus Ellmer[10], Mattis Fondell[11], Claudia Draxl[2], and Renske M. van der Veen[1]

[1]Helmholtz-Zentrum Berlin für Materialien und Energie GmbH, Hahn-Meitner-Platz 1, D-14109 Berlin, Germany

[2]Department Physics and CSMB, Humboldt-Universität zu Berlin, Zum Großen Windkanal 2, D-12489 Berlin, Germany

[3]Department of Chemistry, University of Illinois Urbana-Champaign, 505 South Mathews Avenue, Urbana, Illinois 61801, United States

[4]Supercomputing Department, Zuse Institute Berlin (ZIB), Takustraße 7, 14195 Berlin, Germany

[5]Institute of Optics and Atomic Physics, Technische Universität Berlin, Hardenbergstraße 36, 10623 Berlin, Germany

[6]Chemical Sciences and Engineering Division, Argonne National Laboratory, 9700 S. Cass Avenue, Lemont, Illinois 60439, United States

[7]Department of Materials Science and Engineering, Northwestern University, 2220 Campus Drive, Evanston, Illinois 60208, United States

[8]Université Côte d'Azur, CNRS, CRHEA, rue Bernard Grégory, Sophia Antipolis, 06560 Valbonne, France

[9]Majulab, International Research Laboratory IRL 3654, CNRS, Université Côte d'Azur, Sorbonne Université, National University of Singapore, Nanyang Technological University, Singapore, Singapore

[10]Optotransmitter-Umweltschutz-Technologie (OUT) e.V., Köpenicker Strasse 325, Haus 201, 12555 Berlin, Germany

[11]Helmholtz-Zentrum für Materialien und Energie, Institute for Methods and Instrumentation for Synchrotron Radiation Research, Albert-Einstein-Strasse 15, D-12489 Berlin, Germany

March 24, 2025

*Both authors contributed equally to this work.

Contents

1 Theory

1.1 Constrained density functional theory

The Kohn-Sham (KS) equations provide a practical method for determining the ground-state density of a many-electron system in the external potential of the atomic nuclei. Every KS state $\psi_{i\mathbf{k}}(\mathbf{r})$ is an eigenfunction of the KS Hamiltonian with the corresponding eigenenergy $\epsilon_{i\mathbf{k}}$:

$$\left[-\frac{\nabla^2}{2} + v_{\mathrm{KS}}(\mathbf{r})\right]\psi_{i\mathbf{k}}(\mathbf{r}) = \epsilon_{i\mathbf{k}}\psi_{i\mathbf{k}}(\mathbf{r}), \tag{1}$$

where $\mathbf{k}$ denotes the wavevector, and $v_{\mathrm{KS}}(\mathbf{r})$, the KS potential. The ground state electron density $n_0(\mathbf{r})$ is expressed in terms of $\psi_{i\mathbf{k}}(\mathbf{r})$ as:

$$n_0(\mathbf{r}) = \sum_{\mathbf{k}} w_{\mathbf{k}} \sum_i f^0_{i\mathbf{k}} |\psi_{i\mathbf{k}}(\mathbf{r})|^2, \tag{2}$$

where $w_{\mathbf{k}}$ is the weight of $\mathbf{k}$-point, and $f^0_{i\mathbf{k}}$ is the occupation number of the KS state labeled with $i\mathbf{k}$.

Excited states are modeled by considering that electrons have been promoted to empty states, leaving holes in the previously occupied states. In this approach, the excited-state electron density $n(\mathbf{r})$ is given by:

$$n(\mathbf{r}) = n_0(\mathbf{r}) + n_e(\mathbf{r}) - n_h(\mathbf{r}), \tag{3}$$

where $n_e(\mathbf{r})$ and $n_h(\mathbf{r})$ are the density of excited electrons and holes, respectively.

In constrained density functional theory (cDFT), as implemented in **`exciting`**, the excited-state electron density $n(\mathbf{r})$ is expressed as:

$$n(\mathbf{r}) = \sum_{\mathbf{k}} w_{\mathbf{k}} \sum_i f^0_{i\mathbf{k}} |\psi_{i\mathbf{k}}(\mathbf{r})|^2 + \sum_{c\mathbf{k}} f_{c\mathbf{k}} |\psi_{c\mathbf{k}}(\mathbf{r})|^2 - \sum_{v\mathbf{k}} f_{v\mathbf{k}} |\psi_{v\mathbf{k}}(\mathbf{r})|^2, \tag{4}$$

where v and c represent the indices of valence and conduction states, respectively. The distribution of excited electrons ($f_{c\mathbf{k}}$) and holes ($f_{v\mathbf{k}}$) is constrained based on some physical insight that fulfills the following conditions:

$$\sum_c f_{c\mathbf{k}} = \sum_v f_{v\mathbf{k}}, \tag{5}$$

$$\sum_{c\mathbf{k}} f_{c\mathbf{k}} = N_{\mathrm{exc}}, \tag{6}$$

where N_{exc} represents the number of excitations in a unit cell.

1.2 Real-time time-dependent density functional theory

Real-time time-dependent density functional theory (RT-TDDFT) can be employed to investigate the time evolution of electrons subjected to a time-dependent perturbation, such as electric or magnetic fields. In RT-TDDFT, a KS state $\psi_{j\mathbf{k}}(\mathbf{r}, t)$ evolves under the equation:

$$\frac{\partial}{\partial t}\psi_{j\mathbf{k}}(\mathbf{r}, t) = -\mathrm{i}\hat{H}(\mathbf{r}, t)\psi_{j\mathbf{k}}(\mathbf{r}, t), \tag{7}$$

where $\hat{H}(\mathbf{r}, t)$ is the time-dependent KS Hamiltonian. Considering that a laser pulse, with an electric field described by the vector potential $\mathbf{A}(t)$, excites the electron system, the corresponding KS Hamiltonian can be expressed as (1):

$$\hat{H}(\mathbf{r}, t) = \frac{1}{2}\left(-\mathrm{i}\nabla + \frac{1}{c}\mathbf{A}(t)\right)^2 + v_{\mathrm{KS}}(\mathbf{r}, t), \tag{8}$$

where $v_{\mathrm{KS}}(\mathbf{r},t)$ is the time-dependent KS potential.

Tracking the creation of electron-hole pairs over time is crucial to understanding the excitation dynamics. In RT-TDDFT, this is determined by projecting $\psi_{i\mathbf{k}}(\mathbf{r},t)$ onto the KS states at the initial time, $\psi_{i\mathbf{k}}(\mathbf{r},0)$. The number of excited electrons at a specific **k**-point within a conduction state c (2) is:

$$f_{c\mathbf{k}}(t) = \sum_i f^0_{i\mathbf{k}} |\langle \psi_{c\mathbf{k}}(0) | \psi_{i\mathbf{k}}(t) \rangle|^2. \tag{9}$$

The number of holes left in a valence state v is:

$$f_{v\mathbf{k}}(t) = f^0_{v\mathbf{k}} - \sum_{i\mathbf{k}} f^0_{i\mathbf{k}} |\langle \psi_{v\mathbf{k}}(0) | \psi_{i\mathbf{k}}(t) \rangle|^2, \tag{10}$$

and the number of excited electrons per unit cell is:

$$N_{\mathrm{exc}}(t) = \sum_{c\mathbf{k}} w_{\mathbf{k}} f_{c\mathbf{k}}(t) = \sum_{v\mathbf{k}} w_{\mathbf{k}} f_{v\mathbf{k}}(t). \tag{11}$$

1.3 Bethe-Salpeter equation

X-ray absorption spectra are computed by solving the Bethe-Salpeter equation (BSE) for the two-particle Green's function. In matrix form, the BSE is mapped onto an effective eigenvalue problem (3):

$$\sum_{o'u'\mathbf{k}'} H^{BSE}_{ou\mathbf{k},o'u'\mathbf{k}'} A^{\lambda}_{o'u'\mathbf{k}'} = E_\lambda A^{\lambda}_{ou\mathbf{k}}, \tag{12}$$

with the eigenenergies E_λ and eigenvectors $A^{\lambda}_{ou\mathbf{k}}$, where o and u label the occupied and unoccupied states, respectively. The H^{BSE} Hamiltonian consists of three contributions:

$$H^{BSE} = H^{diag} + 2H^{x} + H^{dir}. \tag{13}$$

H^{diag} represents the diagonal term, accounting for the single-particle transitions; H^x is the exchange term, which includes the repulsive bare Coulomb interaction $\nu(\mathbf{r},\mathbf{r}')$; and H^{dir} is the direct term containing the attractive screened Coulomb interaction $W(\mathbf{r},\mathbf{r}')$:

$$H^{diag}_{ou\mathbf{k},o'u'\mathbf{k}'} = (\epsilon_{u\mathbf{k}} - \epsilon_{o\mathbf{k}})\, \delta_{oo'} \delta_{uu'} \delta_{\mathbf{k}\mathbf{k}'}, \tag{14}$$

$$H^{x}_{vo\mathbf{k},v'o'\mathbf{k}'} = \int d^3\mathbf{r} d^3\mathbf{r}' \psi_{o\mathbf{k}}(\mathbf{r}) \psi^*_{u\mathbf{k}}(\mathbf{r}) \nu(\mathbf{r},\mathbf{r}') \psi^*_{o'\mathbf{k}'}(\mathbf{r}') \psi_{u'\mathbf{k}'}(\mathbf{r}'), \tag{15}$$

$$H^{dir}_{ou\mathbf{k},o'u'\mathbf{k}'} = -\int d^3\mathbf{r} d^3\mathbf{r}' \psi_{o\mathbf{k}}(\mathbf{r}) \psi^*_{u\mathbf{k}}(\mathbf{r}') W(\mathbf{r},\mathbf{r}') \psi^*_{o'\mathbf{k}'}(\mathbf{r}) \psi_{u'\mathbf{k}'}(\mathbf{r}'). \tag{16}$$

$\nu(\mathbf{r},\mathbf{r}')$ and $W(\mathbf{r},\mathbf{r}')$ stand for the bare and screened Coulomb potentials, respectively. Taking the Fourier transform gives $W(\mathbf{r},\mathbf{r}')$ as:

$$W_{\mathbf{G}\mathbf{G}'}(\mathbf{q}) = 4\pi \frac{\varepsilon^{-1}_{\mathbf{G}\mathbf{G}'}(\mathbf{q},\omega=0)}{|\mathbf{q}+\mathbf{G}||\mathbf{q}+\mathbf{G}'|}, \tag{17}$$

where ε is the microscopic dielectric function given in the random-phase approximation, by

$$\varepsilon_{\mathbf{G}\mathbf{G}'}(\mathbf{q},\omega) = \delta_{\mathbf{G}\mathbf{G}'} - \frac{1}{V} \nu_{\mathbf{G}'}(\mathbf{q}) \sum_{ou\mathbf{k}} \frac{f_{u\mathbf{k}+\mathbf{q}} - f_{o\mathbf{k}}}{\epsilon_{u\mathbf{k}+\mathbf{q}} - \epsilon_{o\mathbf{k}} - \omega} \left[M^{\mathbf{G}}_{ou}(\mathbf{k},\mathbf{q}) \right]^* M^{\mathbf{G}'}_{ou}(\mathbf{k},\mathbf{q}). \tag{18}$$

Here, V denotes the unit cell volume, $f_{o\mathbf{k}}$ represents the occupation factor of state o at wavevector $\mathbf{k}$, and $M_{ou}^{\mathbf{G}}(\mathbf{k},\mathbf{q})$ is the plane-wave matrix element between states o and u (4; 5).

The occupations of excited states, obtained by using cFT and RT-TDDFT, are incorporated here to calculate the Coulomb screening contribution to the spectra. Then, the occupations of excited states are used to calculate the dipole moment to obtain the Pauli blocking contribution to the spectra. The dipole moment matrix (D^*) is given by:

$$\mathrm{D}^* = \mathrm{i}\sqrt{|f_{o\mathbf{k}} - f_{u\mathbf{k}+\mathbf{q}}|} \times \frac{\langle c\mathbf{k}|\hat{\mathbf{p}}|u\mathbf{k}\rangle}{\epsilon_{u\mathbf{k}+\mathbf{q}} - \epsilon_{o\mathbf{k}}}, \tag{19}$$

which enters the transition coefficient t_λ:

$$t_\lambda(0,\mathbf{q}) = -\mathrm{i}\frac{\hat{\mathbf{q}}}{|\mathbf{q}|}\mathbf{X}_\lambda^\dagger \mathrm{D}^*, \tag{20}$$

where $\mathbf{X}_\lambda$ is the resonant part of eigenvectors. The $\beta\beta$ tensor components of the macroscopic dielectric function can be obtained from the transition weights:

$$\varepsilon_M^{\beta\beta}(\omega) = 1 - \frac{8\pi}{V}\sum_\lambda |t_\lambda^\beta|^2 \delta(\omega - E_\lambda). \tag{21}$$

Averaging over the Cartesian components of the macroscopic dielectric function, and decomposing it into real and imaginary parts,

$$\frac{\varepsilon_M^{xx}(\omega) + \varepsilon_M^{yy}(\omega) + \varepsilon_M^{zz}(\omega)}{3} = \varepsilon_1(\omega) + i\varepsilon_2(\omega), \tag{22}$$

allows one to express the absorption coefficient as:

$$\alpha(\omega) = \frac{\omega}{v_{\mathrm{light}}} \cdot \sqrt{2} \cdot \sqrt{\sqrt{\varepsilon_1^2(\omega) + \varepsilon_2^2(\omega)} - \varepsilon_1(\omega)}, \tag{23}$$

where v_{light} is the light speed in vacuum.

2 Sample synthesis and characterization

2.1 ZnO thin film for measurements at the Zn K-edge

2.1.1 Synthesis

The film was deposited by pulsed laser deposition (PLD) from a commercial ZnO target using a PVD Products nanoPLD 1000. The system used a KrF excimer laser ($248\,\mathrm{nm}$) with $\sim 25\,\mathrm{ns}$ pulse duration. Prior to deposition, the deposition chamber was pumped to a base pressure of $\sim 2 \times 10^{-7}$ Torr. The deposition was done at 600°C in a 20 mTorr O_2 atmosphere. A pulse energy of $270\,\mathrm{mJ/pulse}$ was used at a $5\,\mathrm{Hz}$ repetition rate. The laser was focused to a spot of $\sim 1.8\,\mathrm{mm} \times 1.0\,\mathrm{mm}$ ($1.8\,\mathrm{mm}^2$). Approximately $55\,\%$ of the laser energy was lost in the optical train, hence the fluence at the target was $\sim 6.7\,\mathrm{J\,cm^{-2}}$. The target-substrate separation was $80\,\mathrm{mm}$, which yielded a deposition rate of $\sim 0.008\,\mathrm{nm/pulse}$. The substrates, **c**-sapphire, were solvent cleaned with acetone and 2-propanol, then annealed ex situ at 1100°C for 2 hours, before deposition.

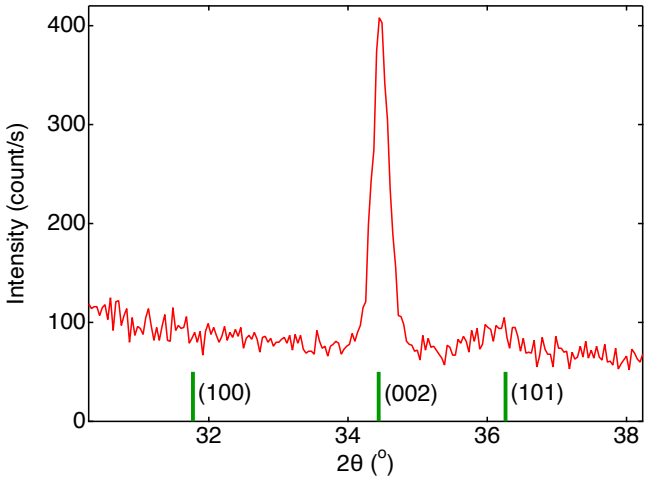

Figure 1: **XRD.** X-ray diffraction pattern of ZnO thin film on **c**-sapphire substrate. Expected diffraction angles for randomly oriented ZnO from reference (6) are shown with vertical green sticks.

2.1.2 X-ray diffraction

X-ray diffraction (XRD) patterns were measured in the Bragg-Brentano geometry with a PANanalytical instrument (at the X-ray CoreLab of the Helmholtz Zentrum Berlin) powered by a copper photocathode (40 kV, 40 mA). The vertical divergence of the input X-ray beam is limited by a $1/16°$ slit and the lateral divergence with $0.04°$ Soller slits. A parallel beam collimator of $0.18°$ is used in front of the detector. Figure 1 shows the XRD pattern of the ZnO thin film on top of a **c**-sapphire substrate. A single (002) reflection is observed, which indicates the uniaxial orientation of the film. The expected position of Bragg reflections from isotropic ZnO are calculated based on the lattice parameters in reference (6) (green sticks in Figure 1). The (002) peak position gives a lattice parameter $c = 5.2026$ Å, in good agreement with previous values on ZnO single crystals (6; 7; 8).

2.1.3 Spectroscopic ellipsometry

The thickness and optical properties of the ZnO thin film were measured by spectroscopic ellipsometry. The ellipsometer is from Sentech (SE850) and the data were analyzed with the SpectraRay 4 software. Figure 2 shows the evolution of the Δ and Ψ ellipsometry parameters with the incidence angle (colored circles). The optical properties of the ZnO dielectric slab were modeled with a three-layer stack composed from top to bottom of: i) a semi-infinite air layer (incidence medium), ii) a ZnO thin film represented by a sum of three Tauc-Lorentz oscillators with a roughness layer at the interface with air, and iii) a **c**-sapphire substrate (semi-infinite layer) with a real refractive index (dispersion) taken from reference (9). Fittings are performed globally at all incidence angles. The results are shown with continuous curves in Figure 2. The fitted parameters are given in Table 1. The real and imaginary parts of the refractive index of the ZnO thin film after deconvolution from the thickness effect of the film are shown in Figure 3. The results of the fitting give for the ZnO thin film alone the permittivity $\epsilon_1/\epsilon_0 = 4.72$, $\epsilon_2/\epsilon_0 = 1.76$ at 355 nm, which are used to calculate the reflectivity and the excitation density of the ZnO thin film (see section 8).

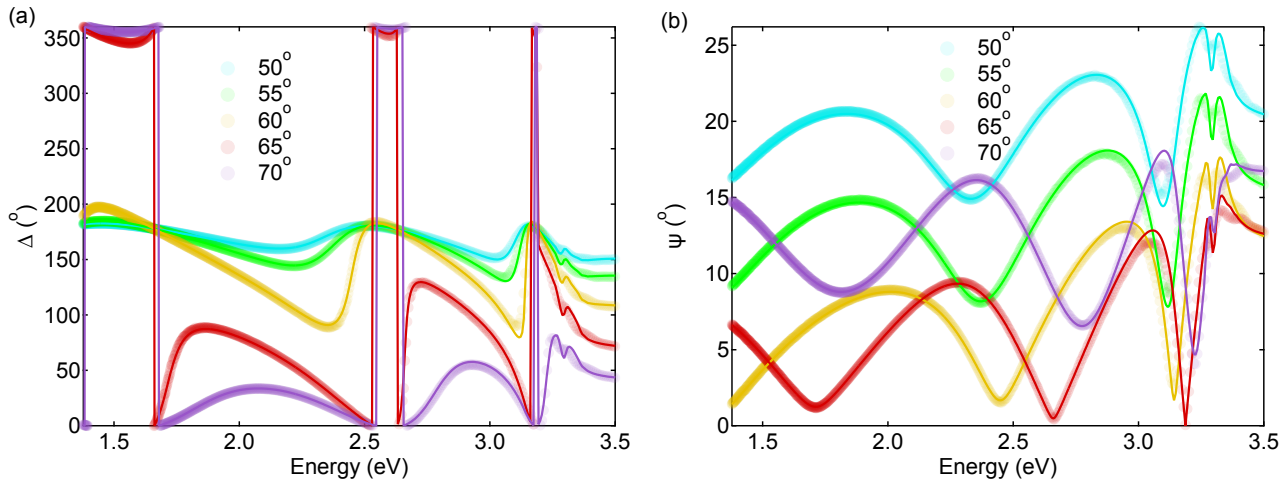

Figure 2: **Angular dependence of spectroscopic ellipsometry constants.** Evolution of (a) Δ and (b) Ψ measured by spectroscopic ellipsometry at various incidences angles on ZnO thin film (colored circles). Fitting results are shown with continuous curves (description of the model in the text).

Parameter	Value	Standard error
Roughness Air/ZnO	16.7 nm	0.1 nm
Fraction of inclusion Air/ZnO	0.45 nm	0.01 nm
ZnO thickness	283 nm	2 nm
ZnO $E_{g,0}$	3.13 eV	0.01 eV
ZnO A_0	117	9
ZnO $E_{0,0}$	3.10 eV	0.02 eV
ZnO C_0	0.45 eV	0.02 eV
ZnO $E_{g,1}$	3.32 eV	0.01 eV
ZnO A_1	606	17
ZnO $E_{0,1}$	3.26 eV	0.01 eV
ZnO C_1	0.055 eV	0.001 eV
ZnO $E_{g,2}$	7.26 eV	0.02 eV
ZnO A_2	214	11
ZnO $E_{0,2}$	3.6 eV	0.2 eV
ZnO C_2	30 eV	15 eV

Table 1: **Spectroscopic ellipsometry fit parameters.** Optimized parameters for the fitting of the permittivity of ZnO thin film by spectroscopic ellipsometry. The Tauc-Lorentz oscillators have the following parameters: band gap (E_g), amplitude (A), resonance energy (E_0), and broadening (C). The three Tauc-Lorentz oscillators have subscripts 0, 1, and 2. The optical dielectric constant $\epsilon_{1,\infty}$=1 is kept constant for the fitting.

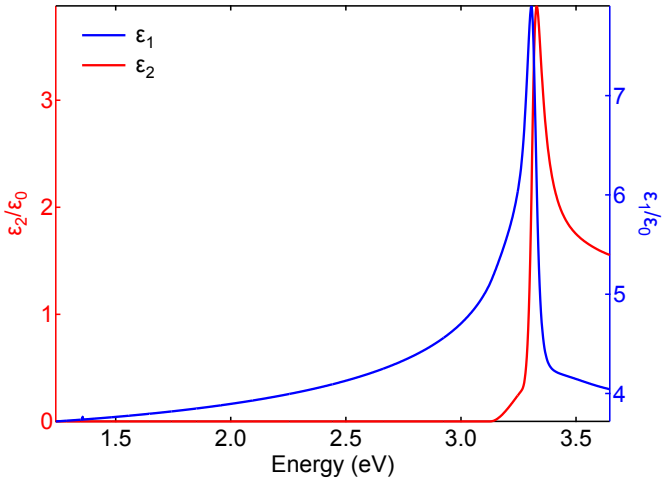

Figure 3: **Fitted permittivity of ZnO thin film.** Real (blue curve) and imaginary (red curve) part of the permittivity obtained by spectroscopic ellipsometry after deconvolution from the spectral oscillations due to the thickness of the ZnO film and contributions from the substrate.

2.2 ZnO thin film for measurements at the Zn L_3-edge

2.2.1 Synthesis

The ZnO thin films grown by plasma-assisted Molecular Beam Epitaxy (MBE) were obtained in a RIBER EPINEAT system. An effusion cell was used for Zn ($99.9999\,\%$) and a radio-frequency plasma cell was used for O ($99.9999\,\%$). The growth was conducted on 100 nm thick SiN membranes on top of Si (500 µm thick) substrates (Norcada), and performed under Zn-rich conditions, mimicking optimized growth condition for **c**-plane O-polar ZnO. The growth rate, O-limited, was $0.345\,\mu\mathrm{m\,h^{-1}}$ ($0.095\,\mathrm{nm\,s^{-1}}$). A two-step growth was applied in order to improve the structural quality of the ZnO thin films. The first layer, about 20 nm thick, was deposited at $450°$C and was then annealed at about $670°$C during 30 minutes. The growth was then restarted using the same growth parameters. Note that the nominal temperatures were not calibrated on the membranes substrates. Such a double-step growth is needed to achieve a good ZnO structural quality, promoting in particular the growth of the (0001) orientation over the most stable (10-11) orientation. The growth rate was calibrated using both cross section measurements by Scanning Electron Microscopy (SEM) and X-ray reflectivity (XRR). The thickness of the sample studied was 400 ± 5 nm, determined by spectroscopic ellipsometry.

ZnO thin films were also deposited by reactive magnetron sputtering in a gas mixture of Ar and O_2 from a ceramic ZnO target. The oxygen partial pressure was adjusted to about $9\,\%$. The total sputtering pressure was 0.5 Pa and the plasma was excited by RF (13.56 MHz) with a discharge power of 50 W. The deposition rate was about $1.8\,\mathrm{nm\,min^{-1}}$. Due to the low discharge voltages (72 to 80 V) the energetic bombardment during the deposition is minimized. The substrates were not intentionally heated during the deposition. Due to the energy input from the plasma and the deposited atoms (Zn, O), a slight temperature increase in the samples occurred ($< 100°$C).

3 XTA experimental setup

Nota Bene: X-ray transient absorption (XTA) spectra in this section are raw data including thermal and non-thermal effects.

3.1 Zn K-edge

The experimental setup used in this work has been previously described in detail in the Supporting Information of reference (10). In brief, X-ray absorption spectra (XAS) and X-ray transient absorption (XTA) spectra were acquired at the 7ID-D beamline of the Advanced Photon Source (APS, Argonne National Laboratories). The spectra were measured in total fluorescence yield with an avalanche photodiode detector (APD0008, FMB Oxford). The X-rays were monochromatized with a double silicon (111) crystal and focused with a pair of Kirkpatrick-Baez (KB) mirrors with the beam footprint imaged on a scintillator crystal in the focal plane of a microscope camera. The X-ray beam was a square-shaped focal spot of $15 \pm 1 \times 39 \pm 1$ µm at normal incidence used for both XAS and XTA measurements. The sample was glued with silver paint (Ted Pella, Pelco®) to a 3D printed plastic sample holder that had a surface at 45° from normal incidence. The X-rays are p-polarized and are at 45° incidence angle at the sample surface (with equal projections along the $(\mathbf{a},\mathbf{b})$ and $\mathbf{c}$ axes of ZnO). The temperature-dependent XAS spectra were recorded with a Linkam THMSG-600 oven (accuracy of 0.01°C). A nitrogen flow was applied onto the sample during the measurement to prevent adsorption and diffusion of carbon impurities and water inside the material and to provide some active cooling to prevent static heating.

The XTA measurements were performed in 24-bunch mode filling pattern with a ring current of 102 mA. The XTA setup has been fully described in reference (11). The photon current detected by the APD is transferred to a boxcar averager (UHF-BOX from Zurich Instruments) controlled remotely with the LabOne user interface. The APD was positioned at 90° from the incident X-ray beam to minimize the contribution from elastic scattering. The pump excitation was performed with a Nd:YVO_4 Duetto laser (Time-Bandwidth products, 1064 nm fundamental wavelength), which delivered ~ 10 ps pulses (FWHM) at 100.266 kHz. The 355 nm excitation wavelength was achieved after frequency doubling and sum frequency generation in two LBO crystals (placed in ovens at $\sim 100^\circ$C for long-term stability and noncritical phase matching). The frequency converted pulses were ~ 10 ps (FWHM) with a spectral bandwidth of 0.1 nm (FWHM). The relative angle between the laser and the X-rays is $\sim 7 \pm 1^\circ$. Spatial overlap between the laser and the X-rays was achieved through a 50 µm diameter pinhole. The laser diameter is 85 ± 5 µm ($1/e^2$) measured by a pinhole scan (Figure 4). The excitation fluences are calculated with the FWHM dimensions of the pump beam (50 ± 3 µm). Fluences are reported with an experimental uncertainty calculated by propagating the uncertainties of the measurements of the laser power (5% of the measured value with a thermal power sensor head) and the uncertainty in laser spot size (see Figure 4). It yields the following equation for the uncertainty over the fluence F with the laser average power P and the laser spot area A,

$$\Delta F = F\sqrt{\frac{\Delta P^2}{P^2} + \frac{\Delta A^2}{A^2}}. \tag{24}$$

The laser is incident on the sample at 52° incidence angle and the incident laser spot size has a circular shape with radius $R = 25 \pm 2$ µm which gives,

$$\Delta F = F\sqrt{\frac{\Delta P^2}{P^2} + \frac{4\Delta R^2}{R^2}}. \tag{25}$$

Temporal overlap of the laser and X-ray pulses was achieved with a fast metal-semiconductor-metal photodetector (Hamamatsu, model G4176-03) connected to a Lecroy digital oscilloscope. An electronic delay was introduced for the laser pulse to achieve a temporal overlap of ~ 10 ps precision. The time delay was set to 100 ± 10 ps between the laser and the X-ray pulses for energy scans. The XTA signal was computed from the difference between the X-ray fluorescence detected with and without the laser pulse divided by the incident X-ray intensity at a given photon energy. The XTA was then normalized

to the XAS edge jump such that the amplitude of the transient is indicative of a normalized change in the XAS with respect to a unitary edge jump (more details in section 5).

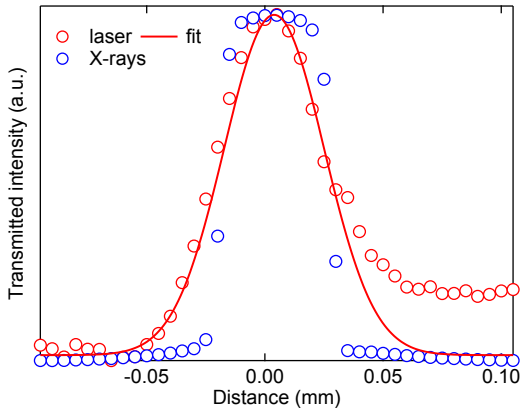

Figure 4: **Spatial overlap at the Zn K-edge.** Laser (red circles) and X-ray (blue circles) beam profiles measured through a $50\,\mu$m diameter pinhole at normal incidence and at focus. A Gaussian fit to the laser profile (red curve) gives a laser spot size of $50 \pm 3\,\mu$m (FWHM) or $85 \pm 5\,\mu$m ($1/e^2$).

The X-ray energy calibration was performed with a zinc foil and compared with the EXAFS Materials reference spectra for metal foils. The energy axes of the XAS spectra also matched a previous work with the same calibration procedure (10). Additionally, the energy scale of XTA measurements on ZnO thin films in this work and in a previous work on ZnO nanorods show that the energy scales are compatible (Figure 5).

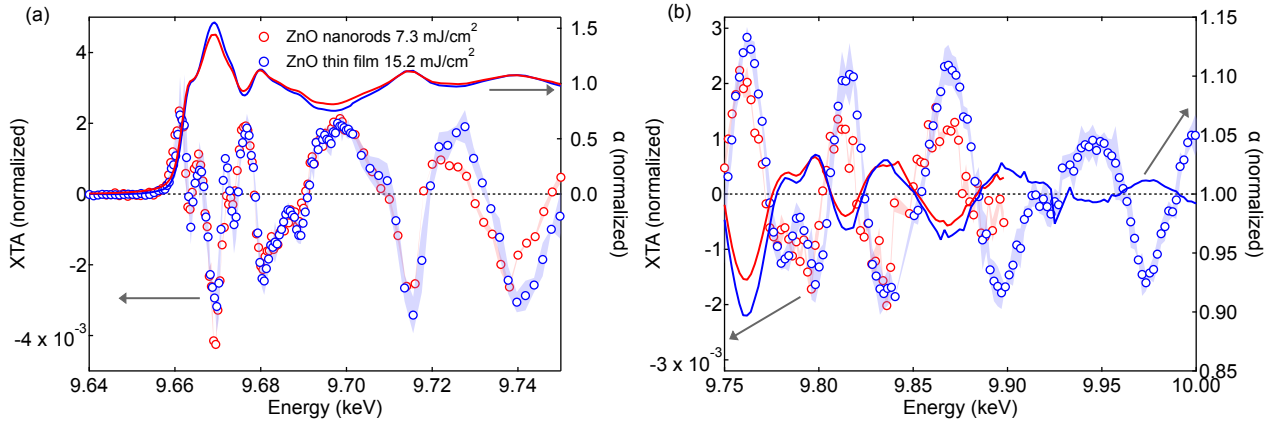

Figure 5: **XTA spectra at the Zn K-edge of ZnO thin films and nanorods.** Comparison between XTA measurements at the Zn K-edge of ZnO nanorods (red circles) and ZnO (0001) thin film (blue circles) at $100\,$ps upon excitation at $355\,$nm in the (a) XANES and (b) EXAFS (left axis). Vertical error bars represent the standard deviation between individual measurements. XAS spectra are shown with continuous curves for reference (right axis). Measurements on ZnO nanorods are reproduced from (10).

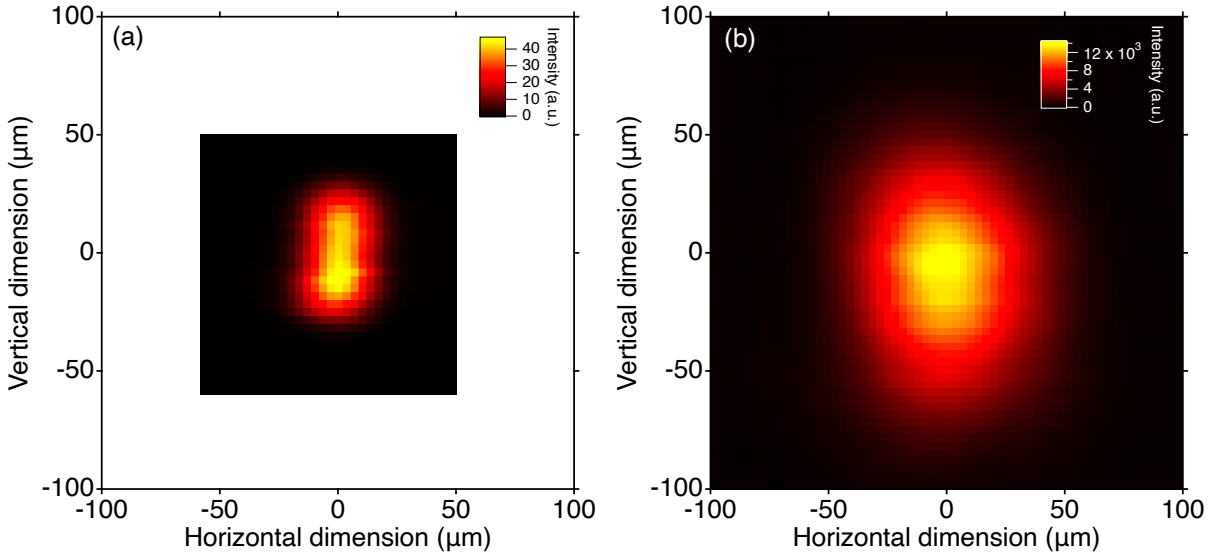

Figure 6: **Beam profiles at the Zn L_3-edge.** Profiles of (a) the X-rays at 1040 eV measured through a 20 µm pinhole (after spatial deconvolution), and (b) the 343 nm pump laser measured on a beam profiler in a focal mirror plane of the sample.

3.2 Zn L_3-edge

XTA spectroscopy measurements at the Zn L_3-edge were conducted at the UE52-SGM beamline of Bessy II in the nmTransmission NEXAFS chamber (12) modified with a sample tip to allow for measurements in transmission of thin film samples. The pump-probe experiment uses the camshaft from the hybrid filling pattern of Bessy II, which yields a temporal resolution of $\sim$ 70–80 ps. The polarization of the X-rays is horizontal, incident at the thin film surface at normal incidence with the polarization in the plane defined by the (**a**,**b**) lattice vectors of the ZnO wurtzite unit cell. The operating vacuum pressure of the chamber was approximately 1×10^{-5} mbar. Initial spatial overlap was determined by visualization of the laser and the X-ray spot on a Ce:YAG screen mounted in the same plane as the sample. The X-ray beam waist is $30 \pm 1 \times 63$ µmpm2 ($1/e^2$ width), measured by deconvoluting an intensity profile measured in transmission of a pinhole with 20 µm diameter (Thorlabs P20HK, Figure 6a). The laser beam waist is measured on a beam profiler (WinCamD-LCM from DataRay) in a focal mirror plane of the sample outside the vacuum chamber (Figure 6b). The final spatial overlap is achieved on the sample by scanning the laser position to achieve the maximum amplitude of the transient signal. Figure 7 shows the horizontal and vertical beam profiles of the laser beam (red circle) and the X-ray beam at the spatial overlap as well as the results of Gaussian fits.

The sample was pumped with 350 fs pulses at 343 nm (third harmonic of the 1030 nm laser fundamental) from a Tangerine laser (Amplitude Systèmes) triggered at 10 kHz by a frequency-divided signal from the synchrotron radiofrequency cavity (p-polarization). The relative angle between the laser and the X-rays is $45 \pm 3°$ with a beam waist of $69 \pm 2 \times 94 \pm 4$ µm ($1/e^2$ width) at the sample position. The incident laser fluence on the sample is calculated from the FWHM of the laser beam waist.

The transmitted X-ray pulses through the sample were collected on a silicon APD (SAR3000, Laser Components) connected to a boxcar integrator (UHF-BOX Zurich Instruments). Electronic gates are set on the camshaft the closest in time to the laser pulse (pumped pulse) and on the camshaft delivered from an earlier synchrotron period by 800 ns on the sample (unpumped camshaft). The transient XTA signal is computed by the difference between the integrated response of the pumped and unpumped

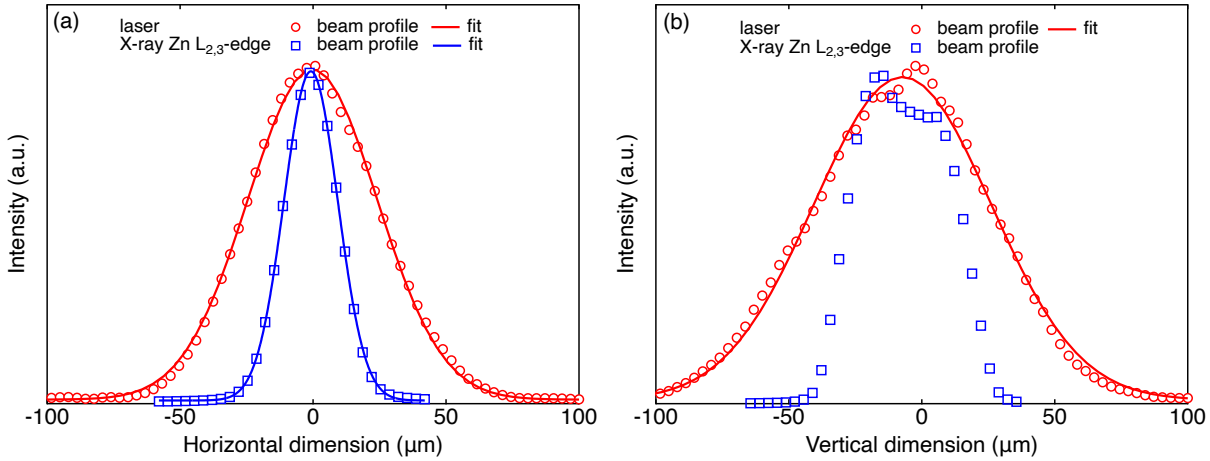

Figure 7: **Spatial overlap at the Zn L_3-edge.** (a) Horizontal and (b) vertical beam profiles at spatial overlap for the laser at 343 nm (red circles) and the X-rays at 1040 eV (blue squares). Gaussian fits the beam profiles show that the laser beam waist is 57 ± 2 µm FWHM (69 ± 2 µm $1/e^2$) horizontally and 78 ± 3 µm FWHM (94 ± 4 µm $1/e^2$) vertically while the X-ray beam is 23 ± 1 µm FWHM (30 ± 1 µm $1/e^2$) horizontally and ~ 46 µm FWHM (~ 63 µm $1/e^2$) vertically.

X-ray pulses through the sample divided by the single bunch current. For the measurement of time traces, a relative time delay is introduced between the laser and X-ray pulses by delaying the laser trigger.

Equilibrium XAS spectra were measured without the laser and with the full intensity of the X-ray beam (given by the total ring current) on a GaAs detector in transmission. The transmitted intensity is normalized by the ring current, which is proportional to the incident X-ray intensity on the sample. The measurement of static heating was performed on the same detector with the laser impinging on the sample at 10 kHz meaning one laser pulse for every 125 synchrotron periods.

4 Kinetics

4.1 Zn K-edge

Time traces at the Zn K-edge at different X-ray energies and excitation fluences are shown in Figure 8. Both in the XANES (Figure 8a,b) and in the EXAFS (Figure 8c), the time traces show that $\sim 80\,\%$ of the XTA signal decays with a time constant $\tau_1 \sim 15$–20 ns for fluences < 25 mJ cm^{-2}. This time constant is similar to the long time constant from a previous measurement at the Zn K-edge of ZnO nanorods (10). Since the transient EXAFS is uniquely described by lattice heating, τ_1 is assigned to heat diffusion in the ZnO thin film. This time constant is in excellent agreement with the short timescale of heat diffusion of ~ 10 ns calculated upon pulse excitation of a ZnO thin film on a glass substrate with a fluence of 30 mJ cm^{-2} (13). It corresponds to heat diffusion in a regime where the carriers have a slightly higher temperature than the lattice, so that lattice heating is still active at the same time as heat diffuses away from the probe volume. At a fluence of ~ 68 mJ cm^{-2}, τ_1 in the EXAFS increases to 33 ns, which indicates that heat diffusion away from the excitation volume has a non-linear behavior with the excitation fluence. The remaining XTA transient signal is fitted with a fixed time constant of $\tau_2 = 10$ µs, much longer than the maximum time delay measured experimentally, which corresponds to heat dissipation away from the ZnO layer, mainly to the substrate. Hence, no decay time constant

measured experimentally is assigned to processes involving carriers such as electron-hole recombination. Time constants of radiative electron-hole recombination are in the range 2–20 ns in ZnO single crystals at room temperature (14; 15; 16; 17), which compares with the time constant of heat diffusion (τ_1). Hence, electron-hole recombination is most likely accidentally synchronous with heat diffusion with the time constant $\tau_1 \sim 15$–20 ns, which cannot be disentangled by fitting the time traces.

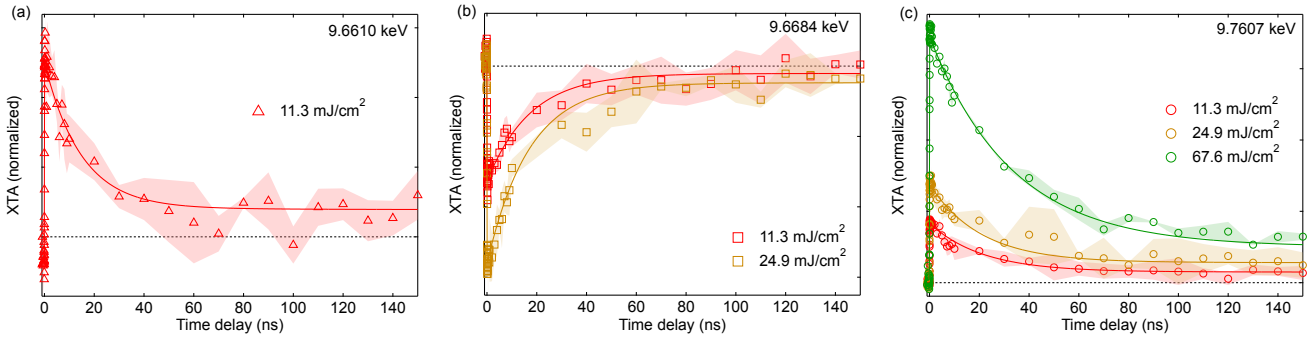

Figure 8: **XTA kinetics at the Zn K-edge.** Evolution of the kinetics at (a) 9.661 keV, (b) 9.6684 keV, and (c) 9.7607 keV at various fluences with 3.49 eV pump photon energy (colored markers). Exponential fits are shown with continuous curves. Shaded areas represented standard deviations between individual measurements.

Photon energy (keV)	fluence (mJ cm^{-2})	$A_1/(A_1+A_2)$	τ_1 (ns)	$A_2/(A_1+A_2)$	τ_2 (ns)
1.028	14	38 ± 2 %	14 ± 5	62 ± 2 %	10000 (fixed)
9.6610	11.3	73 ± 2 %	15 ± 3	27 ± 2 %	10000 (fixed)
9.6684	11.3	90 ± 4 %	17 ± 3	10 ± 4 %	10000 (fixed)
9.6684	24.3	88 ± 1 %	17 ± 2	12 ± 2 %	10000 (fixed)
9.7607	11.3	83 ± 4 %	21 ± 3	17 ± 4 %	10000 (fixed)
9.7607	24.9	80 ± 3 %	21 ± 3	20 ± 3 %	10000 (fixed)
9.7607	67.9	86 ± 1 %	33 ± 1	14 ± 1 %	10000 (fixed)

Table 2: **Fitted kinetic parameters at the Zn L_3- and K-edge of ZnO.** Results of the biexponential fitting of the kinetics at various excitation fluences and X-ray photon energies. The standard errors of the fit parameters are indicated.

Kinetic traces are fitted with a function given by the convolution product of a Gaussian with a FWHM given by the instrument response function (70 ps) and the sum of two exponential decays (parallel decay model) with the decay time constant of the longest component fixed at $\tau_2 = 10$ µs. The amplitude of the individual decay components (A_1 & A_2), the time constant of the shortest component (τ_1) and the position of time zero (half rise of the transient signal) are left as free parameters of the fitting. The fitting is performed in Igor Pro (version 9) with the Levenberg-Marquardt algorithm (18). The individual points are weighted by their standard deviations during the fitting. The fitted parameters are shown in Table 2. The amplitude of each decay component is given as a relative weight (for instance $A_{1,r} = A_1/(A_1+A_2)$ for the shorter-lived specie). The standard error of the amplitude A_1 with a

relative weight $A_{1,r}$ is propagated according to the relation,

$$\Delta A_{1,r} = \left| \frac{A_{1,r}}{A_1 + A_2} \right| \sqrt{\frac{A_2^2}{A_1^2}\sigma_1^2 + \sigma_2^2 - 2\frac{A_2}{A_1}\sigma_{12}} \tag{26}$$

where σ_1 and σ_2 are the standard deviations of A_1 and A_2, respectively, and σ_{12} is the covariance of A_1 and A_2.

4.2 Zn L_3-edge

Figure 9 displays time traces of the XTA at different energy points of the Zn L_3-edge. The time trace at $1028\,\text{eV}$ (green circles) is fitted with a biexponential decay (same model as at the K-edge). The decay time constants are given in Table 2. The value of τ_1 is the same as at the K-edge for similar excitation fluences.

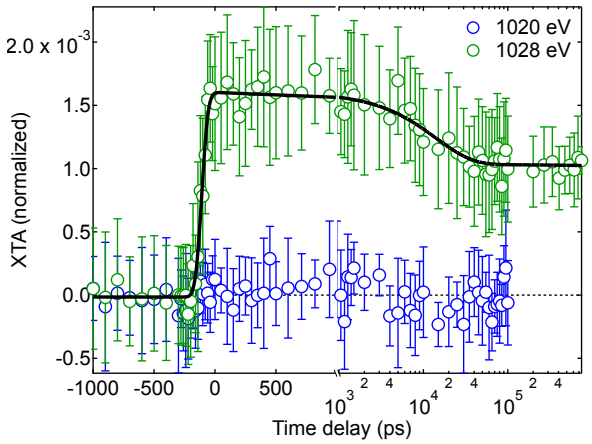

Figure 9: **XTA kinetics at the Zn L_3-edge.** Normalized time traces at the Zn $L_{2,3}$-edge of ZnO at $1020\,\text{eV}$ (blue circles) and $1028\,\text{eV}$ (green circles). The excitation fluence is $14\,\text{mJ}\,\text{cm}^{-2}$. The black curve shows the result of a biexponential decay fitting.

5 Data processing

5.1 XAS spectra data processing

5.1.1 Zn K-edge

The background subtraction, edge jump normalization, and flattening of XAS spectra in the post-edge were performed with the `xraylarch` python package (version 0.9.71) (19). The ionization potential was set to 9673.5 eV and the pre-edge energy range and post-edge energy ranges (relative to the ionization potential) were set between -35 and -25 eV and between 35 and 330 eV relative to the ionization potential, respectively. The pre-edge and post-edge backgrounds were both subtracted with a linear function. Deglitching was applied to a maximum of 3 points per spectra, which originate from diffraction peaks apparent in XAS spectra at specific energy points. Self-absorption effects were not considered in the data analysis since the attenuation length of the most intense K$\alpha_{1,2}$ emission lines (8615.8 and 8638.9 eV (20)) is 35 ± 1 µm ($1/e$) (21), which is several orders of magnitude longer than the thickness of the ZnO thin film (283 ± 2 nm, see SI §2.1.3).

5.1.2 Zn L_3-edge

Edge jump normalization of XAS spectra is performed with our own python script. The pre-edge background is subtracted by fitting a second-order polynomial function between 1000 and 1010 eV while the post-edge normalization and flattening are performed by normalizing the edge jump with respect to a linear fit between 1040 and 1055 eV.

5.2 XTA spectra data processing

After the normalization of individual XTA spectra to the edge jump, statistical outliers 4 standard deviations away from the mean value were removed before averaging and recomputing the standard deviation (performed only once).

6 Thermal effects in XAS and XTA spectra

This section describes the procedure to separate thermal and non-thermal contributions to XTA spectra in two steps: i) the measurement of XAS spectra at different lattice temperatures (section 6.1), and ii) the simulation of XTA spectra upon lattice heating and the comparison with experimental XTA spectra in the EXAFS (section 6.2).

6.1 Temperature-dependent XAS spectra

Temperature-dependent XAS spectra between room temperature (24°C) and 190°C at the Zn K-edge are shown in Figure 10a,b. A clear damping of the EXAFS oscillations around the post-edge absorption line (horizontal dashed line) is observed in the EXAFS at increasing lattice temperatures (black arrows in Figure 10b). The absorption coefficient evolves linearly with the temperature across the whole temperature range (Figure 11). For an accurate subtraction of the thermal contribution to the XTA spectra, the spectra in Figure 10a,b are interpolated using a model-free linear spline function between room temperature and 190°C, which corresponds to the temperature range covered by the experimental data. The standard deviation of the experimental data points is included in the interpolation as a

statistical weight factor. The interpolated XAS spectra are shown in Figure 10c,d as well as the difference XAS spectra between a given temperature and the XAS spectrum at room temperature (24°C) in Figure 10e,f. The standard deviations of individual energy points are conserved for the interpolated data. For the energy points that were not present in the original XAS data but were present in the XTA data, a linear interpolation was performed to obtain the corresponding XAS and its standard deviation.

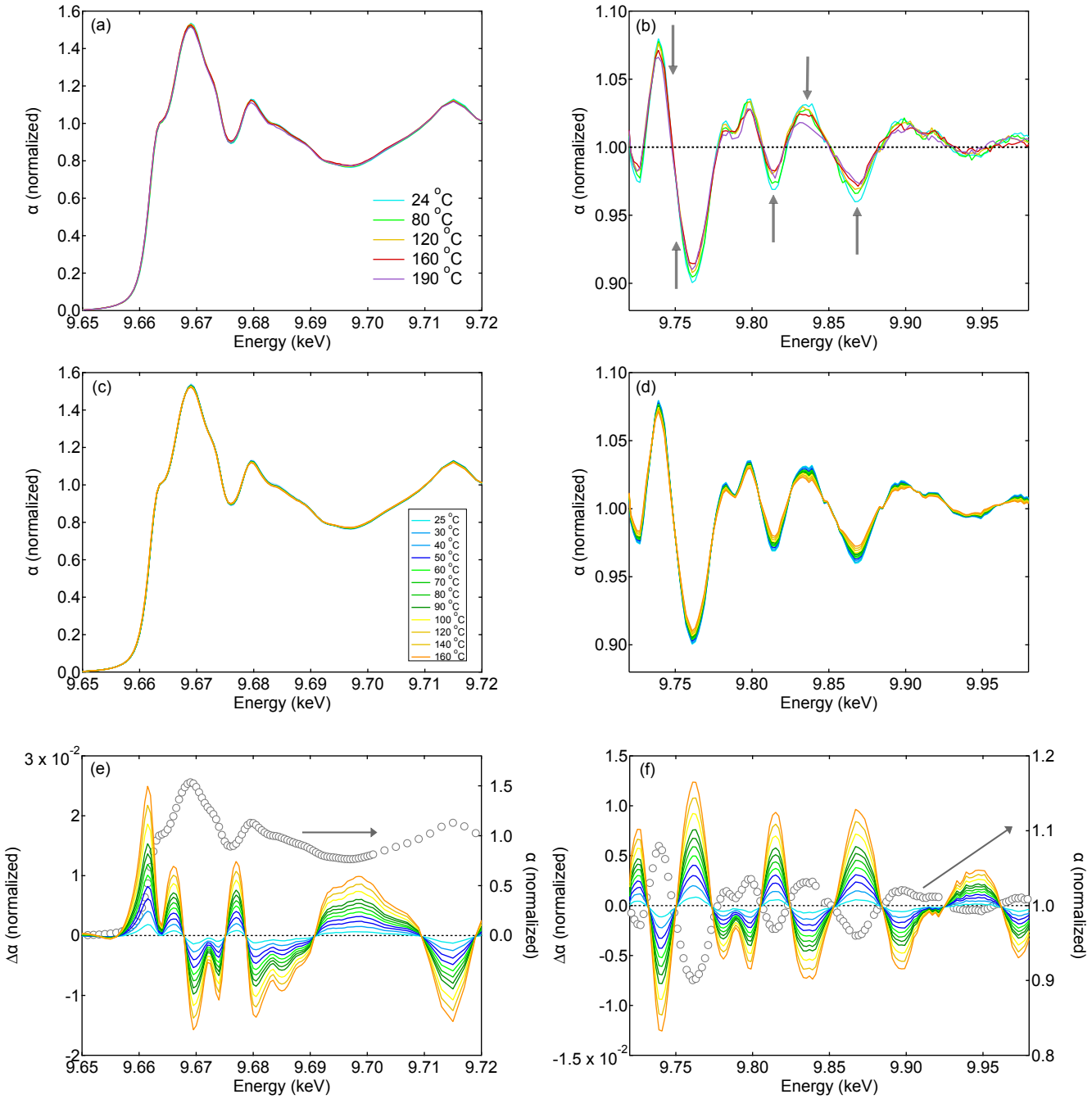

Figure 10: **Temperature-dependence of XAS spectra at the Zn K-edge.** Temperature-dependence of normalized XAS spectra at the Zn K-edge of ZnO in (a,c) the XANES, and (b,d) the EXAFS (colored curves, left axis). The spectra are (a,b) raw data and (c,d) after cubic spline interpolation along a temperature axis. Normalized temperature-difference XAS spectra with respect to the normalized XAS spectrum at $24°$C are shown in (e) the XANES, and (f) the EXAFS (colored curves, left axis). The normalized room temperature XAS spectrum at $24°$C is shown for reference (grey circles, right axis).

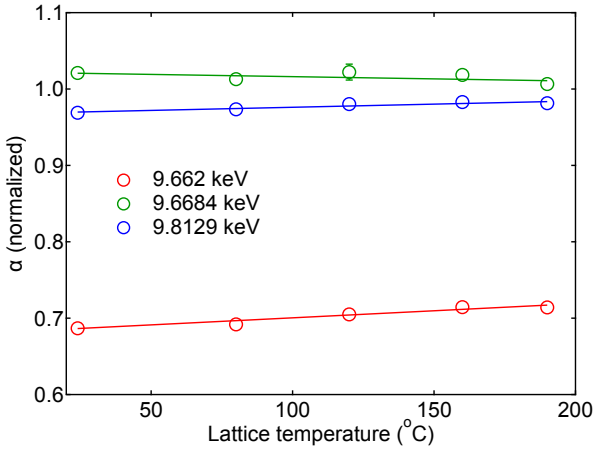

Figure 11: **XAS amplitude with lattice temperature at the Zn K-edge.** Evolution of the XAS amplitude at 9.662 keV (red circles), 9.6684 keV (green circles) and 9.8129 keV (blue circles). Vertical error bars are standard deviations from the measurements. Linear fits are shown with continuous lines.

6.2 Thermal contributions to XTA spectra

6.2.1 General remarks

Transient EXAFS spectra in Figure 12b displays a mirror image lineshape of the equilibrium EXAFS spectrum around a normalized and flattened post-edge absorption line. No phase shift or change in frequency is observed. The damping of EXAFS oscillations is related to increased thermal and/or static disorder, which is phenomenologically described by increased Debye-Waller factors (amplitude of the mean square displacement of the atoms) (22). In the present case, the increased disorder is due to lattice heating as a consequence of energy transfer between the photoexcited carriers and the phonon bath by carrier-phonon coupling on the sub-picosecond timescale (23). At 100 ps time delay, the excess carrier energy has been transferred to the lattice, and the electronic temperature is nearly equal to the hot lattice temperature (24). The hot lattice does not display a sizeable thermal expansion, which would increase the periodicity of the EXAFS oscillations in the excited state. We attribute this effect to the weaker changes induced by < 2 mÅ ($\sim 0.02 \pm 0.01$ %) variations of the average Zn-O bond distance (10) and lattice parameters (8) with respect to the ~ 10 % change of the Debye-Waller factor (6; 8) between 300 and 400 K, which corresponds to the typical lattice heating in the current experiment (*vide infra*).

The unchanged periodicity of the EXAFS oscillations in the photoexcited state excludes the formation of polarons (25) or trapped holes (26) as possible contributions to the transient spectra, since these localized carriers would induce a change of average bond length [1]. The analysis of the XTA spectra at 100 ps time delay is based on the hypothesis that it can be decomposed into a linear combination of thermal and non-thermal signals due to the weak coupling between core excitons and lattice vibrations (detail of the breakdown procedure in 6.2.2). Figure 12b shows that the thermal contribution is dominant in the EXAFS (shaded red area) while the X-ray absorption near-edge structure (XANES) is made of a superposition of thermal and non-thermal (shaded blue area) contributions (Figure 12a). The two contributions in the XANES are distinct with different lineshapes, maxima, and zero-crossing points, in particular between 9.668 and 9.69 keV.

XTA spectroscopy at the Zn K-edge is a bulk-sensitive technique (the penetration depth is ~ 8.5 µm

[1] Polarons can form in ZnO by direct excitation of the mid-gap states but their lifetime is only a few picoseconds (27).

at 9.7 keV (28)), which is insensitive to carrier trapping at the defect-rich surface of the film. More generally, the lattice heating contribution to the XTA signal at 100 ps in the bulk of the ZnO thin film overwhelms any other signal that could originate from local electronic or structural perturbations involving only a few zinc atoms. In previous measurements on nanoparticles, however, the ratio of surface-to-bulk atoms was sufficiently large to observe carrier trapping at the defect-rich surface (26) or the formation of small polarons (29).

6.2.2 Decomposition of thermal and non-thermal contributions to XTA spectra at the Zn K-edge

XAS and XTA spectroscopy are sensitive to both electronic and structural degrees of freedom. In XTA spectra at 100 ps time delay, the effect of the electronic and structural perturbation in the excited state XAS spectrum can be considered independent, which is assigned to the fact that the incoherent thermal motion of the atoms does not perturb the formation of core excitons with a radius comparable to the interatomic bond distances (see main text). Since the EXAFS part of the spectrum is only sensitive to the local atomic displacements around the absorbing atom, it is a fingerprint of the local lattice temperature in the ZnO photoexcited state and can be used to separate thermal and non-thermal effects in XTA spectra. The procedure is in two steps: 1) perform a χ^2-minimization between difference XAS spectra (in Figure 10f) and a given XTA spectrum to find the best description of the hot lattice, and 2) take the difference between the XTA spectrum and the optimized χ^2 difference XAS spectrum. Steps 1) and 2) deliver the *thermal* and *non-thermal* contributions to the XTA spectrum, respectively. The procedure has been described in details in the Supporting Information of reference (10). Figure 13 displays the χ^2-minimized difference XAS spectra (colored curves) together with XTA spectra at different excitation fluences (colored circles with error bars). Figure 14a displays the residuals of the χ^2 minimization and 14b the excited state lattice temperature.

The non-thermal (electronic) part of the XTA spectrum differs from previously published spectra measured with the same polarization on ZnO nanorods (10). The largest difference is the absence of a positive signal in the non-thermal XTA spectrum in Figure 4a of reference (10). We expect this discrepancy may arise from 1) the distribution of nanorod orientations, which broadens the XAS spectrum, 2) larger uncertainties in the subtraction of the thermal contribution to the XTA spectrum due to a lower signal-to-noise ratio, and 3) a larger degree of structural flexibility of the ZnO nanorods, which may lead to some motion of the ZnO nanorods when the temperature increases associated with a change in the X-ray linear dichroism. The latter leads to an inaccurate subtraction of the thermal contribution to the XTA spectrum.

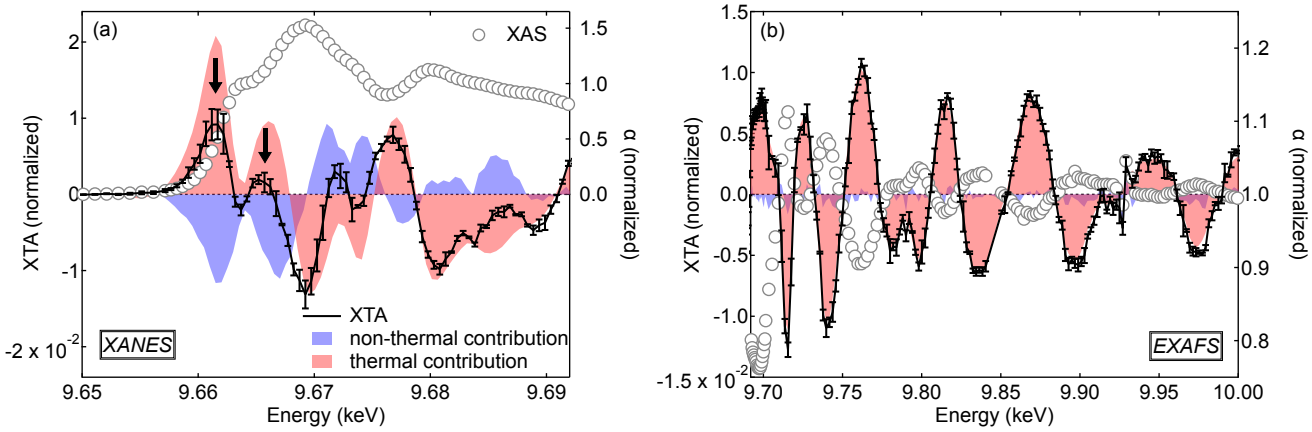

Figure 12: **Decomposition of thermal and non-thermal contributions in the X-ray transient absorption (XTA) spectrum.** Edge-jump normalized XTA spectra at $67.6\,\mathrm{mJ\,cm^{-2}}$ excitation fluence at the Zn K-edge of ZnO (0001) thin films in (a) the XANES and (b) the EXAFS (black curves with error bars, left axis). The XTA spectrum is decomposed into thermal (shaded red area) and non-thermal (shaded blue area) contributions. Time delay is $100\,\mathrm{ps}$, excitation is $3.49\,\mathrm{eV}$, incidence angle is at $45°$ with respect to (0001). Error bars represent standard deviations between individual XTA measurements. The edge-jump normalized XAS spectrum at the Zn K-edge (absorption coefficient, α) is shown with gray circles for reference (right axis).

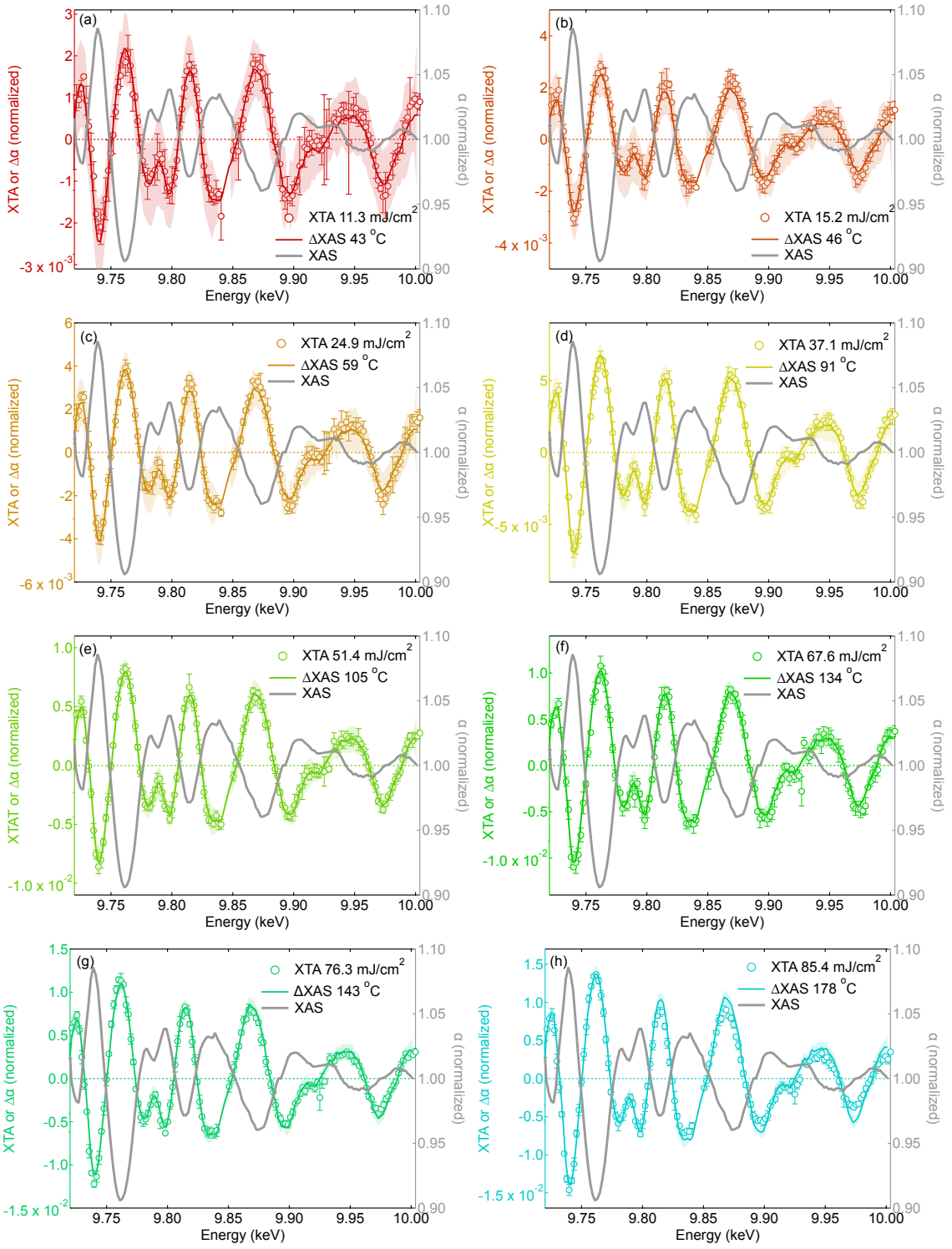

Figure 13: **Thermal contributions to XTA spectra in the EXAFS at the Zn K-edge.** Best agreement after χ^2 minimization between XTA spectra in the EXAFS (colored circles, left axis) and temperature-difference XAS spectra (colored curves, left axis) at the Zn K-edge of ZnO for excitation fluences of (a) 11.3, (b) 15.2, (c) 24.9, (d) 37.1, (e) 51.4, (f) 67.6, (g) 76.3, and (h) $85.4\,\mathrm{mJ\,cm^{-2}}$ ($100\,\mathrm{ps}$ time delay, excitation $3.49\,\mathrm{eV}$). Shaded areas and error bars represent standard deviations between individual measurements. The equilibrium EXAFS spectrum is shown for reference (grey curve, right axis).

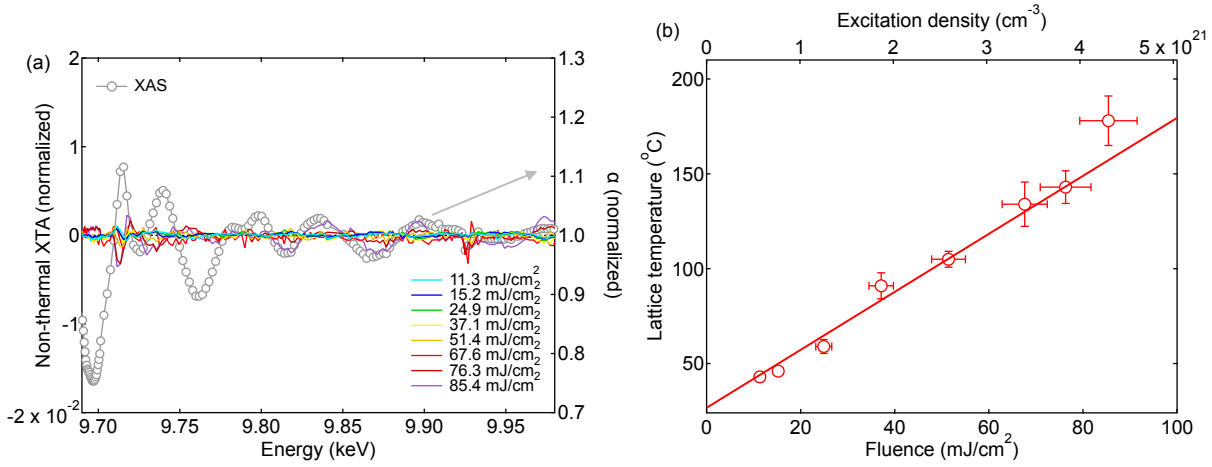

Figure 14: χ^2 **residuals and optimized excited state lattice temperature.** (a) Residuals of the χ^2 minimization between XTA spectra and the best-matched temperature-difference XAS spectra (colored curves, left axis). The equilibrium XAS spectrum is shown for reference (grey circles, right axis). (b) Lattice temperature obtained after χ^2 optimization of the XTA spectra in the EXAFS (red circles). Vertical error bars are the variance of the fitted temperature, horizontal error bars are uncertainties in the estimate of the laser fluence. Linear fit to the data constrained to the vertical error bars (red curve). Top axis is the initial excitation density.

6.2.3 Decomposition of thermal and non-thermal contributions to XTA spectra at the Zn L_3-edge

The subtraction of the lattice heating contribution to the XTA spectrum at the Zn L_3-edge is achieved by performing separate measurements of static heating. The effect of static heating on the XAS is measured with the full X-ray intensity by the difference between two XAS spectra measured with and without laser impinging on the sample (black markers in Figure 15). The laser fluence is the same as in the pump-probe measurements ($14\,\mathrm{mJ\,cm^{-2}}$). Since lattice heating is an overwhelming contribution to XTA spectra at 100 ps far above the absorption edge (10), we make the hypothesis that the XAS difference spectrum obtained from the static heating measurement is a good model of the dynamic heating contribution to the XTA spectrum at 100 ps, with only a constant multiplicative factor correction to apply to get an agreement between the two spectra. This approximation is valid when the dynamic structural fluctuations induced by lattice heating (quantified by the Debye-Waller factor) lead to a linear change of the absorption cross-section with the temperature, which occurs when the lattice temperature is larger than the Debye temperature (30). In ZnO, the Debye temperature (Θ_D) is in the range 370–383 K (6; 8) and since the excited state temperature is $\gg 500$ K at 100 ps (because of the vacuum environment), the linear scaling of the XTA amplitude above the edge with the lattice temperature change is a valid approximation. A multiplicative factor is then applied to the difference XAS spectrum induced by static heating (black circles in Figure 15) to best-match the XTA spectrum between 1045 and 1100 eV (red circles in Figure 16a) by χ^2 minimization. The results are shown in Figure 16a for a best-matched scaling factor of 0.083 for the XAS difference spectrum coming from the static heating measurement. Following the same procedure as at the Zn K-edge, the obtained model of the lattice heating contribution to the XTA spectrum is then subtracted from the XTA spectrum in the near-edge region of the Zn L_3-edge to simulate the non-thermal contribution to the XTA spectrum, shown with a shaded blue curve in Figure 16b and in Figure 7 in the main text.

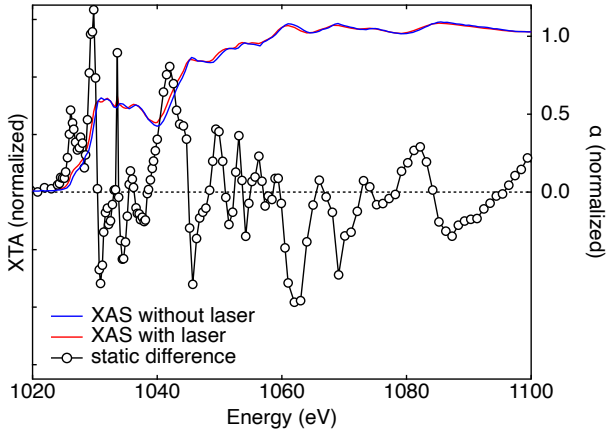

Figure 15: **Laser-induced static heating at the Zn L_3-edge.** Effect of static heating on the XAS spectrum at the Zn L_3-edge of ZnO. Consecutive XAS measurements are performed with (red curve) and without (blue curve) laser impinging on the sample. The difference of the XAS spectra with and without laser irradiation corresponds to the static heating (black circles). Normalization of the XAS spectra and the XAS difference spectra is over the edge jump. The laser fluence is $14\,\mathrm{mJ\,cm^{-2}}$ at $10\,\mathrm{kHz}$.

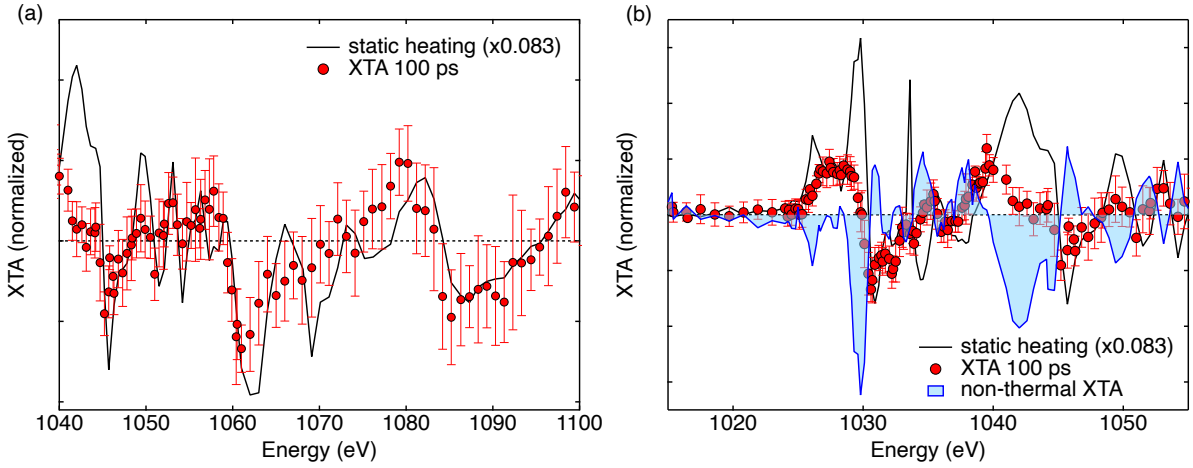

Figure 16: **Thermal and non-thermal contributions to XTA spectra at the Zn L_3-edge.** (a) Best agreement between a scaled XAS difference spectrum corresponding to static heating (black curve, vertical scaling factor of 0.083) and the XTA spectrum at the Zn L_3-edge of ZnO at $100\,\mathrm{ps}$ (red circles with error bars). (b) Difference spectrum between XTA at $100\,\mathrm{ps}$ (red circles) and the lattice heating contribution (black curve) resulting in a simulation of the non-thermal XTA spectrum (shaded blue curve). Error bars correspond to standard deviations between individual measurements. The laser fluence for the XTA measurement is $14\,\mathrm{mJ\,cm^{-2}}$.

6.2.4 Validity of the decomposition of thermal and non-thermal effects

Reported Wannier-Mott exciton radii at the optical gap of ZnO range from 0.9 to $2.34\,\mathrm{nm}$ (31; 32; 33; 34; 35; 36; 37), with the most recent works reporting a value of $\sim 1.4\,\mathrm{nm}$. In contrast, the equilibrium core-exciton radius in the hydrogenoid model is $2\,\text{Å}$ at the Zn K-edge, comparable to the Zn-O bond distance at room temperature ($1.97 - 1.99\,\text{Å}$), which falls into the category of Frenkel excitons (38)

(SI 7.4, Figure 24a). It implies that core excitons are only sensitive to structural dynamics occurring within the first coordination shell. We explain the validity of the separation between thermal (atomic vibrations) and non-thermal (exciton) contributions in the near-edge region of the XTA spectrum to originate from the small dimension of core excitons. This is a fundamental hypothesis made in this work. For instance, since acoustic phonons cause mainly long-range crystal deformations, their coupling to localized core excitons is weak (39). The weak coupling between optical excitons and phonons in covalent semiconductors is a fundamental difference to ionic compounds, in which excitons with binding energies of $\sim 1\,$eV exhibit a strong coupling to phonons (40). Core excitons also have limited coupling with thermal vibrations, since the mean-square displacement of the atoms, quantified by the Debye-Waller factor, is of the order of $2\,\%$ ($\sim 40\,$mÅ) of the equilibrium Zn-O bond distance at room temperature, which is negligible compared to the exciton radii. Due to the short lifetime of the core hole at transition metal K-edges, we exclude the effect of structural motion occurring between the absorption and emission of the X-ray photon on the core exciton spectrum (41). At the Zn L_3-edge, the exciton radius is $1.78\,$Å (SI 7.4, Figure 24b), which is also smaller than the first coordination shell. However, since the lattice temperature is expected to be significantly higher during the Zn L_3-edge experiment due to the vacuum environment and the low thermal contact conductance with the substrate, we expect the incoherent atomic motion to span a significant fraction of the interatomic bond distance, and thus the dynamics of core excitons and atoms cannot be considered as independent as at the K-edge. It likely explains the poorer agreement between the non-thermal XTA and the calculations shown in Figure 2f. Hence, the thermal vibrations encountered here are expected to have a limited impact on the electronic structure of core excitons in covalent semiconductors.

7 Computational supplement for controlling core-exciton screening

7.1 Femtosecond control of core excitons by Coulomb screening

Figure 17 decomposes the XTA spectra into contributions from Coulomb screening (shaded blue area) and Pauli blocking (shaded red curve). Similar to the picosecond spectra, the Coulomb screening by photoexcited carriers dominates the femtosecond spectra. The contribution from Pauli blocking (shaded red area) is nearly two orders of magnitude weaker than the overall XTA spectrum. Pauli blocking (inset of Figure 17) exhibits a prominent negative absorption change around $\sim 9.662\,$keV, differing from the positive signal observed in the picosecond spectra. At short time delays, compared to the electron-phonon scattering time (23), excited electrons occupy a delocalized region across the BZ (Figure 23b), contributing more efficiently to blocking core excitations, consistent with previous femtosecond XTA measurements in semiconductors (42; 43; 44).

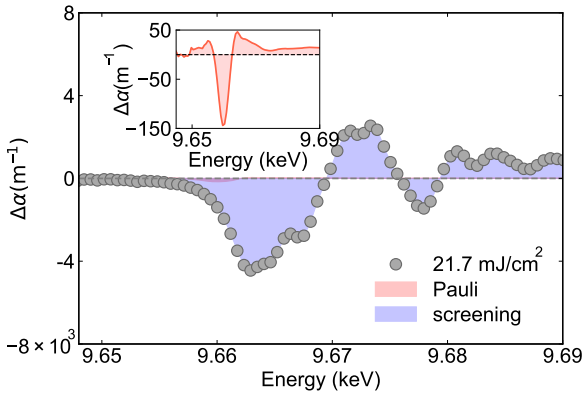

Figure 17: Contributions of Coulomb screening (shaded blue area) and Pauli blocking (shaded red area) from excited carriers to the XTA spectra (black circles) at the Zn K-edge with an excitation fluence of $21.7\,\mathrm{mJ\,cm^{-2}}$ and a time delay of $20\,\mathrm{fs}$. Inset: magnified view of the edge region.

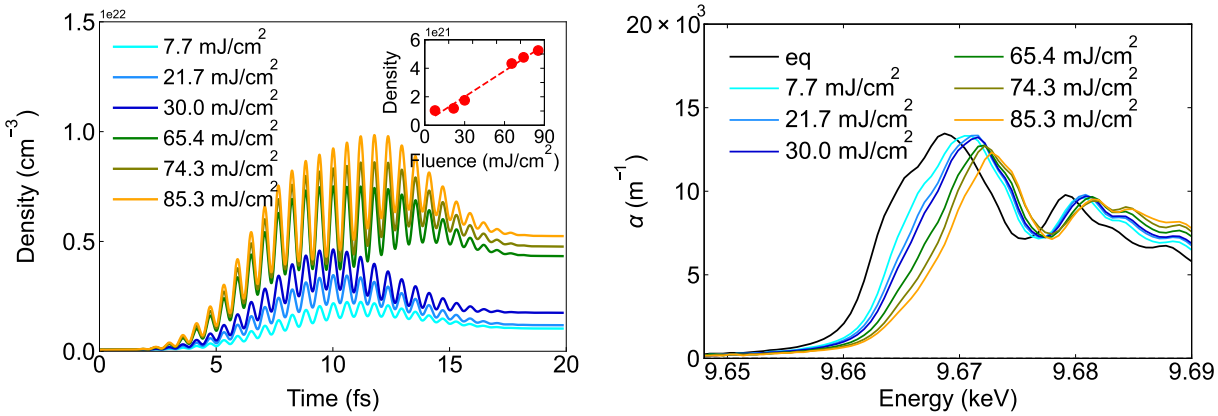

Figure 18: (a) Temporal evolution of the excitation density following pump excitation at various fluences, using a $10\,\mathrm{fs}$ pulse (FWHM) with photon energy $3.49\,\mathrm{eV}$ and polarization aligned along the (100) crystal axis. Inset: Excitation density at $20\,\mathrm{fs}$ as a function of pump fluence. (b) Computed XAS spectra (colored curves) at the Zn K-edge for different pump fluences at $20\,\mathrm{fs}$ on a femtosecond timescale, with the equilibrium XAS spectrum (black curve) shown for reference.

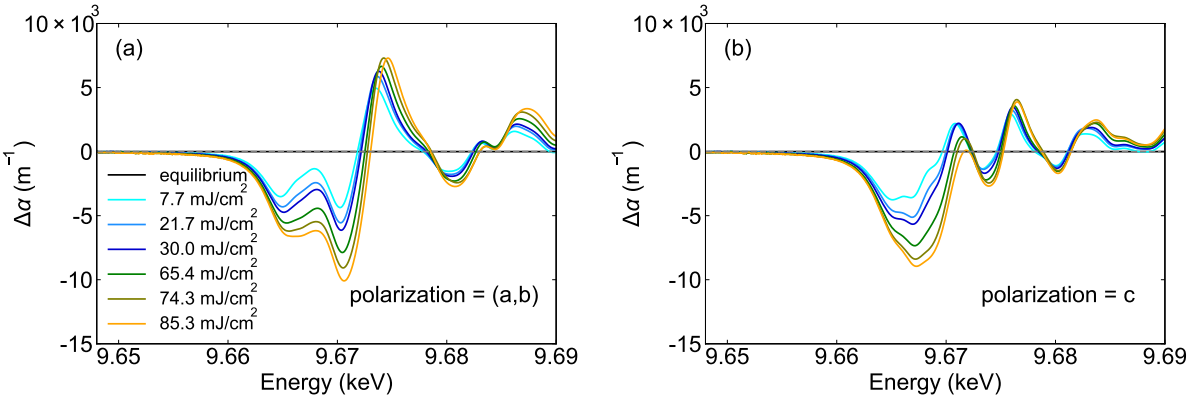

Figure 19: XTA spectra at the Zn K-edge for increasing pump fluences with probe polarization oriented along (a) the (a,b)-plane and (b) the c-axis.

Figure 20 presents the Pearson correlation coefficient as a function of excitation density, comparing the correlation between exciton oscillator strengths obtained from cDFT calculations (blue circles) and RT-TDDFT calculations (red circles). The correlation coefficient quantifies the similarity between the oscillator strength distributions at different excitation densities relative to a reference. For cDFT, the reference is set at an excitation density of $3 \times 10^{17}\,\mathrm{cm}^{-3}$, whereas for RT-TDDFT, the reference corresponds to an excitation density of $1.0 \times 10^{21}\,\mathrm{cm}^{-3}$, equivalent to a fluence of $7.7\,\mathrm{mJ\,cm}^{-2}$. The data reveal that cDFT maintains a high correlation (close to 1) across all examined densities, while RT-TDDFT exhibits a notable decline in correlation as the excitation density increases, indicating significant changes in exciton oscillator strengths under strong excitation conditions.

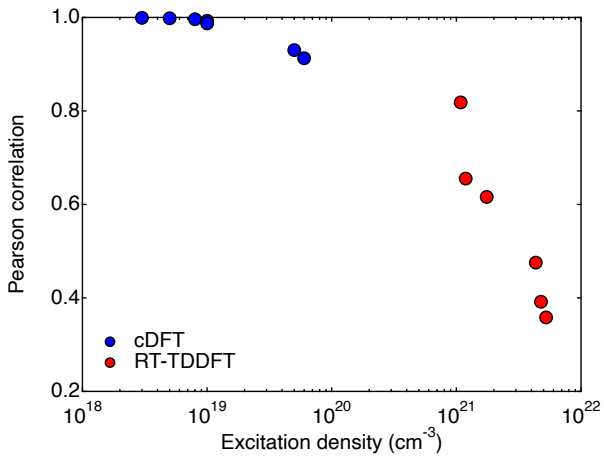

Figure 20: Evolution of the Pearson correlation coefficient between exciton oscillator strengths in cDFT (blue circles) and RT-TDDFFT (red circles). The reference exciton oscillators strengths are for an excitation density of $3 \times 10^{17}\,\mathrm{cm}^{-3}$ with cDFT and $1.0 \times 10^{21}\,\mathrm{cm}^{-3}$ (fluence of $7.7\,\mathrm{mJ\,cm}^{-2}$) with RT-TDDFT.

7.2 Renormalization of single-particle energy gap on picosecond timescale

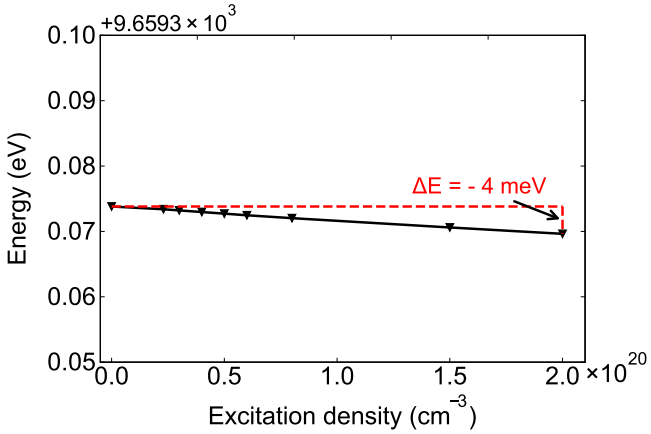

Figure 21: Variation of the single-particle energy gap between the Zn 1s core level and the CBM+1 state at the Γ-point as a function of excitation density. The photoinduced renormalization of this gap remains negligible, with a maximum shift of only 4 meV.

7.3 Electron-hole exchange interaction contribution to XTA spectra

Pauli blocking can be categorized into phase-space filling and short-range exchange interaction contributions (45). Following pump excitation, phase-space filling prohibits X-ray absorption from the Zn 1s core level to the occupied CB, leading to a reduction of the XAS amplitude in the excited state. Similarly, it enhances the X-ray absorption to the unoccupied VB states that are emptied by photoexcitation. Besides, electron-hole exchange interactions prevent two particles (either electrons or holes) with the same spin from occupying the same quantum state. After excitation, the delocalized nature of the photoexcited carriers means that they do not significantly affect the short-range exchange interaction, which relies on the close spatial proximity between particles. The attractive long-range electron-hole Coulomb interaction instead is a prerequisite for the formation of bound excitons. After photoexcitation, the excited carriers screen and thus decrease the electron-hole Coulomb interaction. Here, we refer to the combined effects of phase-space filling and exchange interaction modifications as Pauli blocking, while the screening of the Coulomb interaction is referred to as Coulomb screening. The effect of Pauli blocking (shaded red area), mainly originating from the modification of the exchange interaction due to photoexcited carriers (Figure 22b), is nearly an order of magnitude weaker. The negligible contribution of phase-space filling is related to the localized distribution of excited electrons in the Brillouin zone (BZ) after 100 ps, which only blocks a small fraction of the states contributing to the X-ray absorption transitions at the K-edge (carrier distribution displayed in Figure 23a).

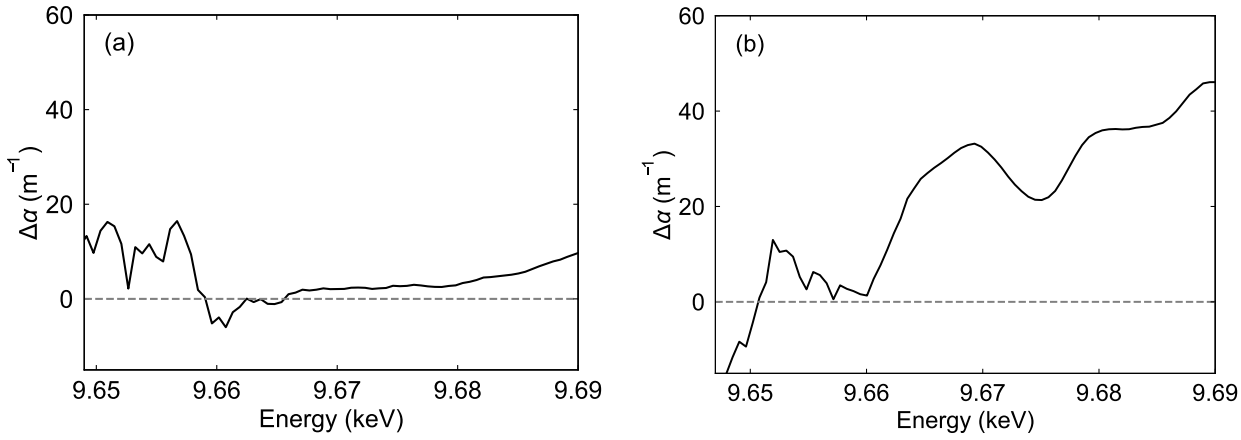

Figure 22: (a) XTA spectra computed within the independent particle approximation (IPA). (b) XTA spectra obtained by further incorporating the electron-hole exchange interaction into the IPA at an excitation density of $5.0 \times 10^{19}\,\mathrm{cm}^{-3}$.

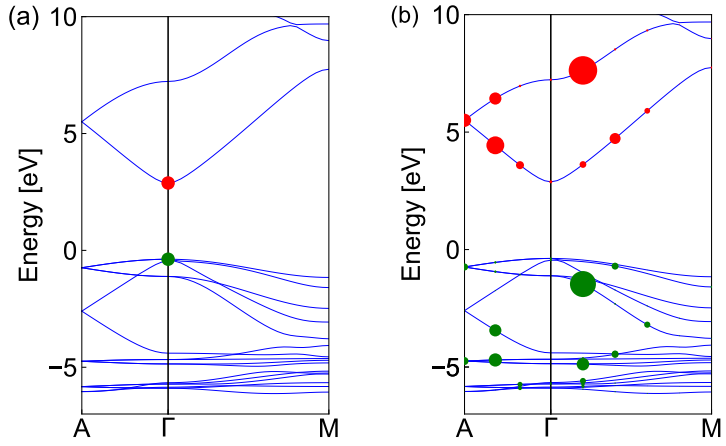

Figure 23: Distribution of excited electrons (red) and holes (green) in the Brillouin zone at time delays of (a) $100\,\mathrm{ps}$ and (b) $20\,\mathrm{fs}$. Panel (a) shows the distribution obtained from cDFT at an excitation density of $2.3 \times 10^{19}\,\mathrm{cm}^{-3}$, while panel (b) presents the distribution from RT-TDDFT simulations with a pump fluence of $74.3\,\mathrm{mJ\,cm}^{-2}$. The size of the circles is proportional to the occupation numbers at the corresponding **k**-points.

7.4 Visualization of the exciton wavefunction in real space

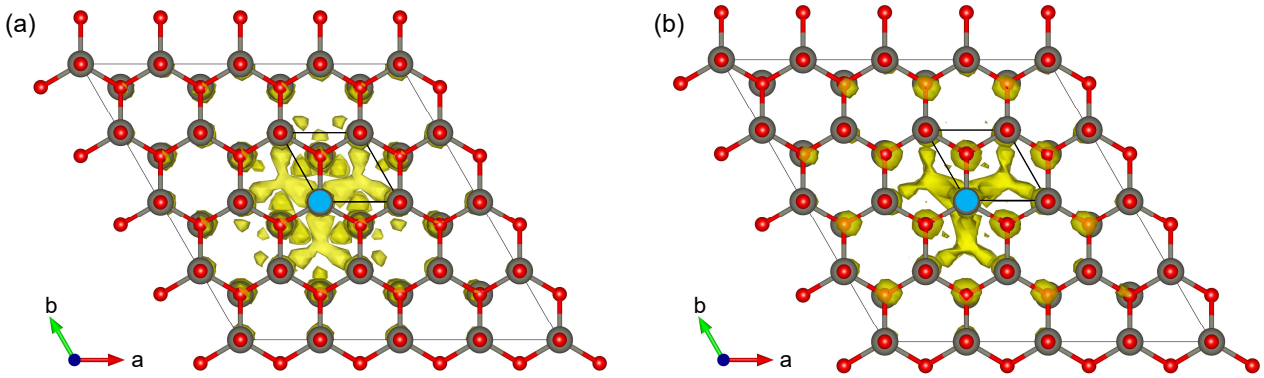

Figure 24: Electron distribution of the lowest-energy core exciton at equilibrium at (a) the K-edge and (b) the L_3-edge. The core-hole positions are marked by blue circles. Zinc and oxygen atoms are shown in gray and red, respectively. The small black box indicates the unit cell. Representations generated with `VESTA` (46).

8 Calculation of the excitation density

8.1 Initial excitation density

The procedure for the calculation of the initial excitation density has been discussed extensively in the Supporting Information of reference (10). We neglect the birefringence of ZnO which leads to variations of the permittivity between $7\,\%$ and $11\,\%$ for the real and imaginary parts between the extraordinary and ordinary polarizations at the pump wavelength, respectively (47). Hence, the relative permittivity of ZnO is obtained from spectroscopic ellipsometry measurements (see section 2.1.3), which yield $\epsilon_1 = 4.72$ and $\epsilon_2 = 1.76$ at the pump wavelength of $355\,\text{nm}$ ($3.49\,\text{eV}$) and at room temperature. The permittivity converts into a complex refractive index with the real part $n = 2.21$ and the imaginary part $\kappa = 0.40$. The reflectance for the p-polarized pump at $45°$ incidence angle is 0.2 and the absorption coefficient is $\alpha = 1.41 \times 10^7\,\text{m}^{-1}$ corresponding to a penetration depth of $71\,\text{nm}$. In these conditions, the laser pulse energy is fully absorbed by the sample. We have shown earlier how the excitation density gets homogeneous in the probe volume at $100\,\text{ps}$ (10). Finally, the initial excitation density n_0 delivered by the pump pulse is calculated with the relation,

$$n_0 = F\frac{(1-R)}{h\nu t} \tag{27}$$

where R is the reflectivity, F is the fluence (corrected for the incidence angle), $h\nu$ is the pump photon energy ($3.49\,\text{eV}$) and t is the sample thickness (obtained by spectroscopic ellipsometry, see section 2.1.3). Equation 27 accounts for reflectance losses as well as the film thickness at an oblique incidence angle. The conversion between the incident fluence and the initial excitation density is given in Table 3.

F ($\mathrm{mJ\,cm^{-2}}$)	n_0 ($\mathrm{cm^{-3}}$)	$n(100\,\mathrm{ps})$ ($\mathrm{cm^{-3}}$)
11.3	5.7×10^{20}	2.4×10^{19}
15.2	7.7×10^{20}	3.2×10^{19}
24.9	1.3×10^{21}	5.3×10^{19}
37.1	1.9×10^{21}	7.9×10^{19}
51.4	2.6×10^{21}	1.1×10^{20}
67.6	3.4×10^{21}	1.4×10^{20}
76.3	3.9×10^{21}	1.6×10^{20}
85.4	4.3×10^{21}	1.8×10^{20}

Table 3: **Fluence and excitation densities.** Equivalence between the incident laser fluence (F), the initial excitation density from the absorbed pump pulse energy (n_0), and the excitation density at $100\,\mathrm{ps}$ ($n(100\,\mathrm{ps})$).

8.2 Decay of the excitation density at $100\,\mathrm{ps}$

The excitation density over time is calculated numerically in order to account for the similar timescales of excitation density increase upon absorption of the pump pulse, and decrease due to electron-hole population decay. The time evolution of the excitation density is obtained from a finite difference method evaluation of the differential equation:

$$\frac{dn}{dt} = -kn + \dot{S} \tag{28}$$

where k is the effective rate of free carrier decay and $\dot{S}$ the source term derived from a gaussian source $S(t) = n_0 e^{-t^2/(2\sigma^2)}$ with n_0 the peak excitation density of the pump pulse (such that $n_{exc} = \int_{-\infty}^{\infty} n_0 e^{-t^2/(2\sigma^2)} dt$ with n_{exc} the total excitation density delivered by the pump pulse and calculated from the absorbed fluence), and σ the duration of the pump pulse related to the full width at half maximum (FWHM, $10\,\mathrm{ps}$) with $\sigma = \mathrm{FWHM}/(2\sqrt{2\ln 2})$. The effective decay rate is taken from previous time-resolved photoluminescence measurements at the band gap using a similar pulse duration and photon energy, which shows that the overwhelming contribution to the decay is an exponential decay with time constant in the range $15 - 40\,\mathrm{ps}$ (48; 49; 50), which is set to $31\,\mathrm{ps}$ in this work corresponding to the average decay time of the free exciton emission at room temperature in reference (49). The results of the simulation are displayed in Figure 25a. The evolution of the excitation density at $100\,\mathrm{ps}$ displays a linear evolution with the excitation fluence (Figure 25b). The values of the excitation density at $100\,\mathrm{ps}$ ($n_0(100\,\mathrm{ps})$) are reported in Table 3.

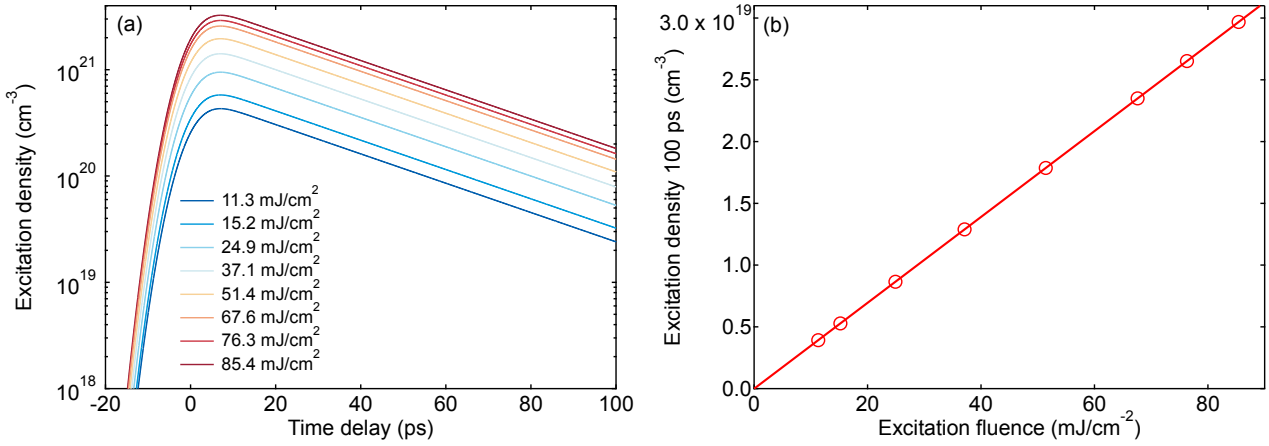

Figure 25: **Time evolution of the excitation density.** (a) Numerical evaluation of the excitation density with time. (b) Excitation density at 100 ps (circles) with linear fit.

9 Fluence dependence of the XTA spectra

9.1 Zn K-edge

Figure 26 shows XTA spectra measured at increasing excitation fluences focusing on the XANES (panel a) and the EXAFS (panel b). Figure 27a shows the evolution of the XTA amplitude at 9.661 keV (red circles) and 9.6684 keV (green circles). Figure 27b shows the evolution of the local slope (derivative) of XTA amplitude with the excitation fluence in panel a.

Non-thermal XTA spectra are modelled by assuming that the non-equilibrium XAS spectrum is equal to the equilibrium XAS spectrum but shifted to higher energies. The results obtained by matching the amplitude of the first negative feature at 9.661 keV are displayed as colored circles in Figure **??**b. The main features of the experimental non-thermal XTA spectra are qualitatively reproduced by applying positive shifts between 10 and 40 meV. While the blue shift accounts for the overall shape of the transient spectra, indicating an increase in the energy of core-level transitions upon photoexcitation, clearly, more subtle amplitude changes cannot be simulated in this way.

Figure 4 in the main text shows a fluence dependence of the integral amplitude of the XTA spectrum. To illustrate its non-linear behavior, we have linearly fitted the data points at fluences below 50 mJ cm^{-2}, corresponding to the fluence above which the *total* XTA amplitude (including thermal contributions) and its derivative deviate from linear behavior (SI 9, Figure 27).

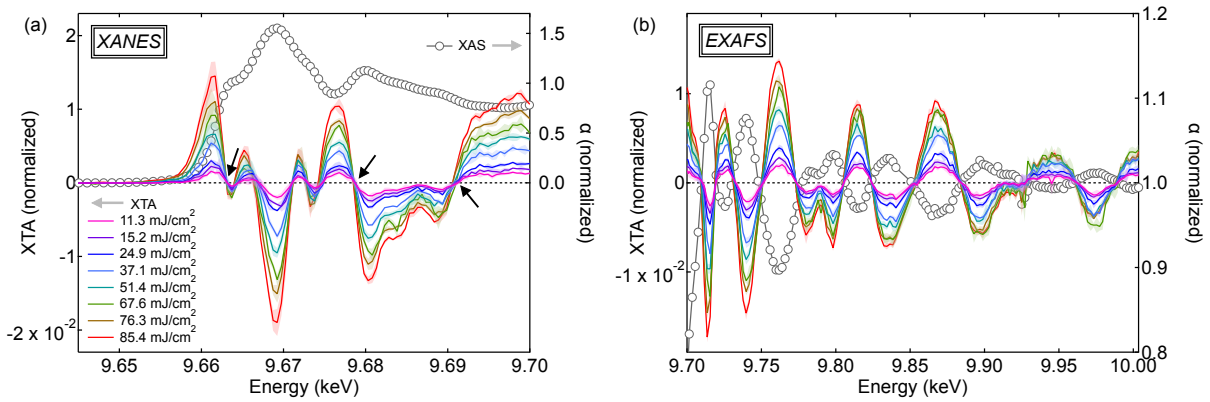

Figure 26: Edge-jump normalized XTA spectra at various excitation fluences at the Zn K-edge of ZnO (0001) thin films in (a) the XANES and (b) the EXAFS regions (colored curves, left axis) for a time delay of 100 ps, an excitation energy of 3.49 eV, and an incidence angle of $45°$ with respect to (0001). Shaded areas represent standard deviations between individual measurements, black arrows indicate isosbestic points in the XANES. The edge-jump normalized XAS spectrum at the Zn K-edge (absorption coefficient, α) is shown with gray circles for reference (right axis).

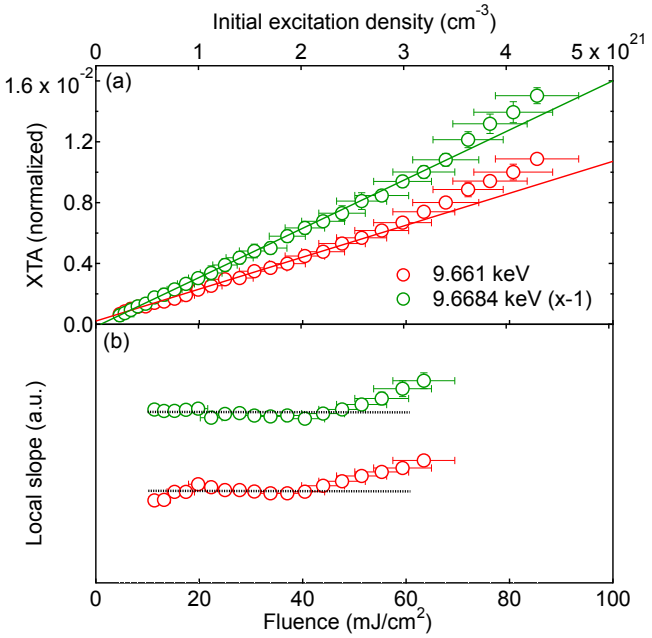

Figure 27: Evolution of (a) the XTA amplitude and (b) the local slope (derivative) of the XTA amplitude with the excitation fluence at 100 ps at 9.661 keV (red circles) and 9.6684 keV (green circles). Vertical error bars represent standard deviations between individual measurements, horizontal error bars are uncertainties in the calculation of the laser fluence. Linear fits in (a) include data points at fluences $< 50\,\mathrm{mJ\,cm^{-2}}$ and are weighted by the standard deviations. The local slope in (b) is based on a linear fit of 11 consecutive data points in panel (a) around a mean fluence. Horizontal black dashed lines are guides to the eye.

9.2 Zn L_3-edge

Under vacuum, the ZnO thin film undergoes a large static heat load, which does not recover between consecutive laser pulses. Because of the difference operation between the pumped and the unpumped response to compute the XTA signal, this contribution is removed. The amplitude of the XTA signal did not show any sign of non-linearity within the accessible pump fluences (Figure 29a) with similar lineshapes between 100 ps and 100 ns time delay (Figure 29b). Samples grown by molecular beam epitaxy (MBE) or radio frequency sputtering (RF) did not exhibit XTA spectra with significant differences in the near-edge region. However, larger differences appear above the edge, which are assigned to different laser-induced heat loads on the two samples (Figure 30).

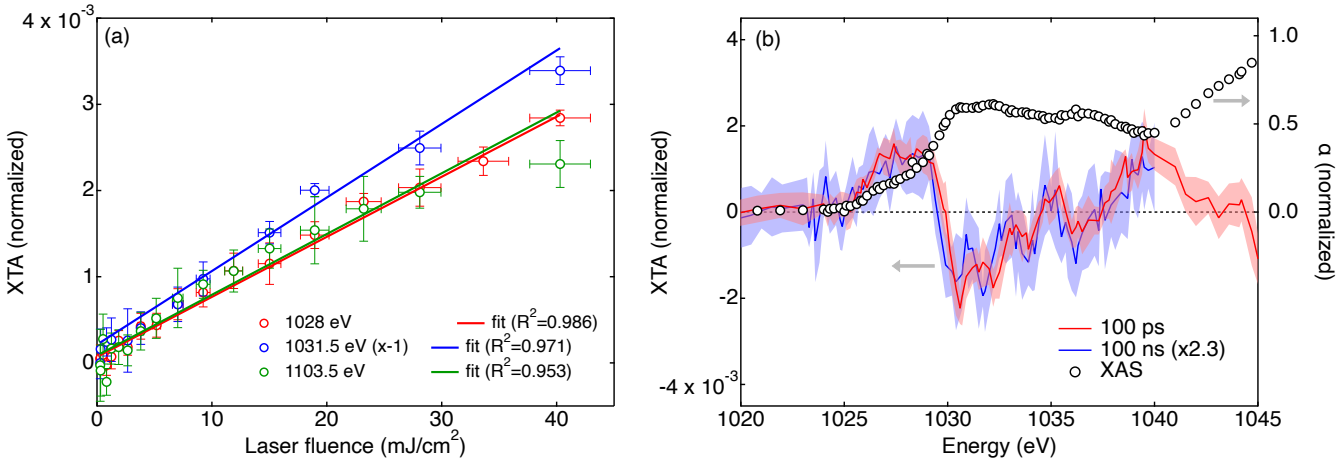

Figure 29: **Fluence dependence and measurements at later time delays at the Zn L_3-edge.** (a) Fluence dependence at the Zn L_3-edge of ZnO (colored circles, 100 ps time delay). Selected energy points are 1028 eV (red circles), 1031.5 eV (blue circles) and 1103.5 eV (green circles). The vertical error bars represent standard deviations between individual measurements and the horizontal error bars represent the uncertainty in the calculation of the laser fluence. Linear fits are weighted by the standard deviation of the measurement. (b) Comparison between normalized XTA spectra at 100 ps (red curve) and 100 ns (blue curve, rescaled by a factor 2.3). Shaded areas represent standard deviations between individual measurements. The XAS is shown with black circles for reference. The laser excitation fluence is $14\,\mathrm{mJ\,cm^{-2}}$. Note that the fluence dependence includes both thermal and non-thermal effects.

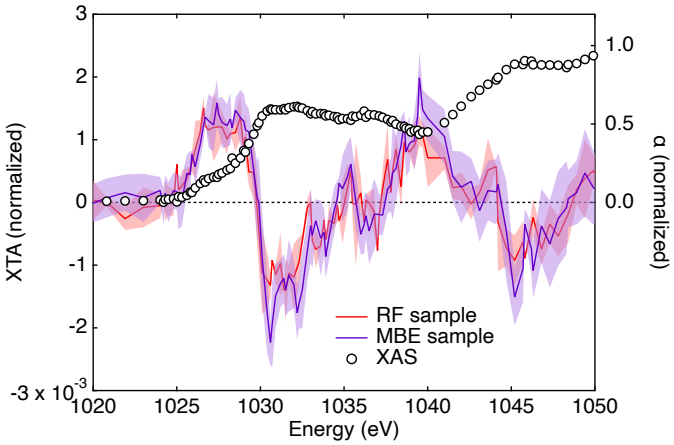

Figure 30: **Effect of sample morphology on XTA spectra at the Zn L_3-edge.** Effect of the sample growth method on the XTA spectrum at 100 ps under 355 nm excitation: radiofrequency sputtering (RF, red shaded curve) and molecular beam epitaxy (MBE, purple shaded curve). The XAS spectrum of the MBE sample is shown with black circles for reference. Shaded areas in the XTA spectra represent standard deviations between individual measurements. The laser excitation fluence is $14\,\mathrm{mJ\,cm^{-2}}$.

References

[1] K. Yabana, T. Sugiyama, Y. Shinohara, T. Otobe, and G. F. Bertsch, Physical Review B **85**, 045134 (2012).

[2] R. Rodrigues Pela and C. Draxl, Electronic Structure **3**, 037001 (2021).

[3] M. Rohlfing and S. G. Louie, Physical Review B **62**, 4927 (2000).

[4] C. Vorwerk, C. Cocchi, and C. Draxl, Physical Review B **95**, 155121 (2017).

[5] C. Vorwerk, B. Aurich, C. Cocchi, and C. Draxl, Electronic Structure **1**, 037001 (2019).

[6] K. Kihara and G. Donnay, Canadian Mineralogist **23**, 647 (1985).

[7] A. A. Khan, Acta Crystallographica Section A **24**, 403 (1968).

[8] J. Albertsson, S. C. Abrahams, and A. Kvick, Acta Crystallographica Section B Structural Science **45**, 34 (1989).

[9] E. D. Palik, *Optical Parameters for the Materials in HOC I and HOC II*, Vol. Handbook of Optical Constants of Solids (Elsevier, 1997) pp. 313–335.

[10] T. C. Rossi, C. P. Dykstra, T. N. Haddock, R. Wallick, J. H. Burke, C. M. Gentle, G. Doumy, A. M. March, and R. M. van der Veen, Nano Letters **21**, 9534 (2021).

[11] A. M. March, A. Stickrath, G. Doumy, E. P. Kanter, B. Krässig, S. H. Southworth, K. Attenkofer, C. A. Kurtz, L. X. Chen, and L. Young, Review of Scientific Instruments **82**, 073110 (2011).

[12] M. Fondell, S. Eckert, R. M. Jay, C. Weniger, W. Quevedo, J. Niskanen, B. Kennedy, F. Sorgenfrei, D. Schick, E. Giangrisostomi, R. Ovsyannikov, K. Adamczyk, N. Huse, P. Wernet, R. Mitzner, and A. Föhlisch, Structural Dynamics **4**, 054902 (2017).

[13] D. Scorticati, G. R. B. E. Römer, A. J. Huis in't Veld, and D. F. de Lange, Journal of Heat Transfer **138**, 031301 (2016).

[14] T. Skettrup and L. Lidholt, Solid State Communications **6**, 589 (1968).

[15] T. Koida, S. F. Chichibu, A. Uedono, A. Tsukazaki, M. Kawasaki, T. Sota, Y. Segawa, and H. Koinuma, Applied Physics Letters **82**, 532 (2003).

[16] A. Teke, U. Özgür, S. Doğan, X. Gu, H. Morkoç, B. Nemeth, J. Nause, and H. Everitt, Physical Review B **70**, 195207 (2004).

[17] S. F. Chichibu, T. Onuma, M. Kubota, A. Uedono, T. Sota, A. Tsukazaki, A. Ohtomo, and M. Kawasaki, Journal of Applied Physics **99**, 093505 (2006).

[18] K. Levenberg, Quarterly of Applied Mathematics **2**, 164 (1944).

[19] M. Newville, Journal of Physics: Conference Series **430**, 012007 (2013).

[20] J. A. Bearden, Reviews of Modern Physics **39**, 78 (1967).

[21] B. Henke, E. Gullikson, and J. Davis, Atomic Data and Nuclear Data Tables **54**, 181 (1993).

[22] J. Timoshenko, A. Anspoks, A. Kalinko, and A. Kuzmin, Acta Materialia **79**, 194 (2014).

[23] V. P. Zhukov, P. M. Echenique, and E. V. Chulkov, Physical Review B **82**, 094302 (2010).

[24] A. Othonos, Journal of Applied Physics **83**, 1789 (1998).

[25] H. Sezen, H. Shang, F. Bebensee, C. Yang, M. Buchholz, A. Nefedov, S. Heissler, C. Carbogno, M. Scheffler, P. Rinke, and C. Wöll, Nature Communications **6**, 6901 (2015).

[26] T. J. Penfold, J. Szlachetko, F. G. Santomauro, A. Britz, W. Gawelda, G. Doumy, A. M. March, S. H. Southworth, J. Rittmann, R. Abela, M. Chergui, and C. J. Milne, Nature Communications **9**, 478 (2018).

[27] Q. Liu, H. Chen, Z. Wang, and Y. Weng, The Journal of Physical Chemistry C **125**, 10274 (2021).

[28] J. H. Hubbell, *Photon cross sections, attenuation coefficients, and energy absorption coefficients from 10 keV to 100 GeV* (National Bureau of Standards, Gaithersburg, MD, 1969) p. 193.

[29] J. E. Katz, X. Zhang, K. Attenkofer, K. W. Chapman, C. Frandsen, P. Zarzycki, K. M. Rosso, R. W. Falcone, G. A. Waychunas, and B. Gilbert, Science **337**, 1200 (2012).

[30] J. Als-Nielsen and D. McMorrow, *Elements of Modern X-ray Physics* (Wiley, UCL, London, United Kingdom Hoboken, NJ, USA, 2011).

[31] V. A. Fonoberov and A. A. Balandin, Physical Review B **70**, 195410 (2004).

[32] B. Gil and A. V. Kavokin, Applied Physics Letters **81**, 748 (2002).

[33] R. E. Dietz, J. J. Hopfield, and D. G. Thomas, Journal of Applied Physics **32**, 2282 (1961).

[34] L. Wischmeier, C. Bekeny, T. Voss, S. Börner, and W. Schade, physica status solidi (b) **243**, 919 (2006).

[35] D. Thomas, Journal of Physics and Chemistry of Solids **15**, 86 (1960).

[36] Y. S. Park, C. W. Litton, T. C. Collins, and D. C. Reynolds, Physical Review **143**, 512 (1966).

[37] R. T. Senger and K. K. Bajaj, Physical Review B **68**, 045313 (2003).

[38] J. Frenkel, Physical Review **37**, 1276 (1931).

[39] M. J. Cherukara, K. Sasikumar, W. Cha, B. Narayanan, S. J. Leake, E. M. Dufresne, T. Peterka, I. McNulty, H. Wen, S. K. R. S. Sankaranarayanan, and R. J. Harder, Nano Letters **17**, 1102–1108 (2017).

[40] R. D. Carson and S. E. Schnatterly, Physical Review Letters **59**, 319–322 (1987).

[41] G. D. Mahan, *Many-Particle Physics* (Springer Science & Business Media, 2012) p. 1032.

[42] M. Verkamp, J. Leveillee, A. Sharma, M.-F. Lin, A. Schleife, and J. Vura-Weis, Journal of the American Chemical Society **143**, 20176 (2021).

[43] S. K. Cushing, A. Lee, I. J. Porter, L. M. Carneiro, H.-T. Chang, M. Zürch, and S. R. Leone, The Journal of Physical Chemistry C **123**, 3343 (2019).

[44] S. H. Park, A. Katoch, K. H. Chae, S. Gautam, P. Miedema, S. W. Cho, M. Kim, R.-P. Wang, M. Lazemi, F. de Groot, and S. Kwon, Nature Communications **13**, 2531 (2022).

[45] K.-C. Je, M. Choi, S.-Y. Yim, J. S. Ahn, and S.-H. Park, Physical Review B **66**, 155312 (2002).

[46] K. Momma and F. Izumi, Journal of Applied Crystallography **44**, 1272 (2011).

[47] S. Shokhovets, L. Spieß, and G. Gobsch, Journal of Applied Physics **107**, 023509 (2010).

[48] B. Guo, Z. Ye, and K. Wong, Journal of Crystal Growth **253**, 252 (2003).

[49] S.-K. Lee, B.-J. Kwon, Y.-H. Cho, H.-J. Ko, and T. Yao, Physical Review B **84**, 139 (2011).

[50] A. Chernikov, M. Koch, B. Laumer, T. A. Wassner, M. Eickhoff, S. W. Koch, and S. Chatterjee, Applied Physics Letters **99**, 9 (2011).